Astronomy & Astrophysics

A 3D view of dwarf galaxies with *Gaia* and VLT/FLAMES

I. The Sculptor dwarf spheroidal[★,★★]

Eline Tolstoy[1], Ása Skúladóttir[2,3], Giuseppina Battaglia[4,5], Anthony G. A. Brown[6], Davide Massari[7,1],
Michael J. Irwin[8], Else Starkenburg[1], Stefania Salvadori[2,3], Vanessa Hill[9], Pascale Jablonka[10,11], Maurizio Salaris[12],
Thom van Essen[1], Carla Olsthoorn[1], Amina Helmi[1], and John Pritchard[13]

[1] Kapteyn Astronomical Institute, University of Groningen, PO Box 800, 9700 AV Groningen, The Netherlands
e-mail: etolstoy@astro.rug.nl
[2] Dipartimento di Fisica e Astronomia, Universitá degli Studi di Firenze, Via G. Sansone 1, 50019 Sesto Fiorentino, Italy
[3] INAF/Osservatorio Astrofisico di Arcetri, Largo E. Fermi 5, 50125 Firenze, Italy
[4] Instituto de Astrofísica de Canarias, Calle Vía Láctea s/n, 38206 La Laguna, Tenerife, Spain
[5] Universidad de La Laguna, Avda. Astrofísico Fco. Sánchez, 38205 La Laguna, Tenerife, Spain
[6] Leiden Observatory, Leiden University, Niels Bohrweg 2, 2333 CA Leiden, The Netherlands
[7] INAF – Osservatorio di Astrofisica e Scienza dello Spazio di Bologna, Via Gobetti 93/3, 40129 Bologna, Italy
[8] Institute of Astronomy, Madingley Road, Cambridge CB3 0HA, UK
[9] Laboratoire Lagrange, Université de Nice Sophia Antipolis, CNRS, Observatoire de la Côte d'Azur,
CS34229 06304 Nice Cedex 4, France
[10] Institute of Physics, Laboratory of Astrophysics, Ecole Polytechnique Fédérale de Lausanne (EPFL), Observatoire de Sauverny,
1290 Versoix, Switzerland
[11] GEPI, Observatoire de Paris, CNRS, Université Paris Diderot, 92125 Meudon Cedex, France
[12] Astrophysics Research Institute, Liverpool John Moores University, 146 Brownlow Hill, Liverpool L3 5RF, UK
[13] European Southern Observatory, Karl-Schwarzschild-Str. 2, 85748 Garching bei München, Germany

ABSTRACT

We present a new homogeneous survey of VLT/FLAMES LR8 line-of-sight radial velocities ($v_{\rm los}$) for 1604 resolved red giant branch stars in the Sculptor dwarf spheroidal galaxy. In addition, we provide reliable Ca II triplet metallicities, [Fe/H], for 1339 of these stars. From this combination of new observations (2257 individual spectra) with ESO archival data (2389 spectra), we obtain the largest and most complete sample of $v_{\rm los}$ and [Fe/H] measurements for individual stars in any dwarf galaxy. Our sample includes VLT/FLAMES LR8 spectra for ~55% of the red giant branch stars at $G < 20$ from *Gaia* DR3, and >70% of the brightest stars, $G < 18.75$. Our spectroscopic velocities are combined with *Gaia* DR3 proper motions and parallax measurements for a new and more precise membership analysis. We look again at the global characteristics of Sculptor, deriving a mean metallicity of $\langle$[Fe/H]$\rangle = -1.82 \pm 0.45$ and a mean line-of-sight velocity of $\langle v_{\rm los} \rangle = +111.2 \pm 0.25$ km s^{-1}. There is a clear metallicity gradient in Sculptor, -0.7 deg dex^{-1}, with the most metal-rich population being the most centrally concentrated. Furthermore, the most metal-poor population in Sculptor, [Fe/H] < -2.5, appears to show kinematic properties distinct from the rest of the stellar population. Finally, we combine our results with the exquisite *Gaia* DR3 multi-colour photometry to further investigate the colour-magnitude diagram of the resolved stellar population in Sculptor. Our detailed analysis shows a similar global picture as previous studies, but with much more precise detail, revealing that Sculptor has more complex properties than previously thought. This survey emphasises the role of the stellar spectroscopy technique and this galaxy as a benchmark system for modelling galaxy formation and evolution on small scales.

Key words. galaxies: dwarf – galaxies: individual: Sculptor dwarf spheroidal – stars: abundances – galaxies: evolution

1. Introduction

Classical dwarf spheroidals (dSphs) such as Sculptor occupy the faint end of the galaxy luminosity function. In the immediate vicinity of the Milky Way, they are fully resolved star by star down to luminosities well below the oldest main sequence turnoff. As apparently strongly dark-matter-dominated systems, they are powerful test beds for models of dark matter, as well as the processes that drive star formation and chemical enrichment at early times. Compared to larger and more massive galaxies, dwarf galaxies are much more sensitive to the energetic process of star formation and stellar feedback. Thus, they allow us to distinguish what is universal in galaxy evolution from what are more stochastic processes at work in small systems. We are able to study dSphs in detail because the total number of stars is large enough that their dynamic and chemical properties can be traced using many hundreds of individual red giant branch (RGB) stars, which can be accurately compared to detailed predictions from models and simulations.

The *Gaia* mission (Gaia Collaboration 2016, 2023) has provided a breakthrough in our understanding of resolved stellar

---

★ Full Tables E.1 and E.2 are only available at the CDS via anonymous ftp to cdsarc.cds.unistra.fr (130.79.128.5) or via https://cdsarc.cds.unistra.fr/viz-bin/cat/J/A+A/675/A49
★★ Based on VLT/FLAMES observations collected at the European Organisation for Astronomical Research (ESO) in the Southern Hemisphere under programmes 171.B-0588, 072.D-0245, 076.B-0391, 079.B-0435, 593.D-0309, 098.D-0160, 0100.B-0337, 0101.D-0210, 0101.B-0189, and 0102.B-0786.

populations in and around the Milky Way, and even in nearby dwarf galaxies. *Gaia* has no equal when it comes to astrometry, which, combined with its exquisite photometry, is a uniquely powerful tool for accurately selecting and analysing member stars throughout nearby resolved dwarf galaxies, especially in the sparse outskirts. However, *Gaia* will not provide complete line-of-sight (los) velocities, v_{los}, or metallicities for individual stars in most of the satellite dwarf galaxies. This provides a clear motivation to create the most complete and homogeneous survey of 3D velocities and metallicities of RGB stars in dSphs down to the magnitude limit that matches *Gaia* astrometry. This allows accurate comparisons with 3D dynamical models and in turn allows us to look for rotation and tidal effects and determine the relation with the orbit around the Milky Way, while also providing a more complete understanding of the chemical evolution over time within these systems.

The Sculptor dSph is a satellite of the Milky Way at a distance of 83.9 kpc (Martínez-Vázquez et al. 2015). It is a key test case for models of galaxy formation and evolution as it is a metal-poor fossil from the early Universe. It stopped forming stars ~8–10 Gyr ago (de Boer et al. 2012; Bettinelli et al. 2019; de los Reyes et al. 2022). Thus it provides a clear vision of ancient times, unobscured by recent star formation episodes. Sculptor has been studied extensively in relation to: its star formation history (SFH; e.g. Monkiewicz et al. 1999; Dolphin 2002; de Boer et al. 2012; Weisz et al. 2014; Savino et al. 2018; Bettinelli et al. 2019); the chemical abundances of its stellar population (e.g. Norris & Bessell 1978; Shetrone et al. 1998, 2003; Tolstoy et al. 2003; Geisler et al. 2005; Clementini et al. 2005; Kirby et al. 2009, 2019; Starkenburg et al. 2013; Skúladóttir et al. 2015a,b, 2017, 2018, 2019, 2020, 2021; Jablonka et al. 2015; Simon et al. 2015; Lardo et al. 2016; Chiti et al. 2018; Hill et al. 2019; Salgado et al. 2019; Reichert et al. 2020; Tang et al. 2023); and its kinematics (e.g. Queloz et al. 1995; Tolstoy et al. 2001, 2004; Battaglia et al. 2008a; Walker et al. 2009; Zhu et al. 2016; Massari et al. 2018; Iorio et al. 2019). In addition, the RR Lyrae variable stars in the Sculptor dSph have long been studied (e.g. Baade & Hubble 1939; Kaluzny et al. 1995; Martínez-Vázquez et al. 2015).

Despite the simplicity of Sculptor's SFH, and its spheroidal structure, its kinematics are surprisingly complex. Previous studies have revealed at least two distinct components, distinguished by different metallicity distributions, spatial distributions, and kinematics (e.g. Tolstoy et al. 2004; Battaglia et al. 2008a; Walker & Peñarrubia 2011; Breddels et al. 2013; Breddels & Helmi 2013). By determining the SFH of Sculptor at different radii, de Boer et al. (2012) showed that older, more metal-poor populations are present throughout the galaxy, while younger, more metal-rich stars tend to be more centrally concentrated, confirming what was also shown by other tracers of specific stellar populations (e.g. Hurley-Keller et al. 1999; Harbeck et al. 2001; Tolstoy et al. 2004). These observational results mean that it is not straightforward to model the properties of the Sculptor dSph and uniquely determine the evolutionary path that led to the galaxy we see today (e.g. Battaglia et al. 2008b; Salvadori et al. 2008, 2015; Łokas 2009; Revaz et al. 2009; Agnello & Evans 2012; Romano & Starkenburg 2013; Zhu et al. 2016; Strigari et al. 2017; de los Reyes et al. 2022).

The existing spectroscopic datasets of Sculptor provide metallicities ([Fe/H]) and los velocities (v_{los}) that are neither complete nor homogeneous. The incompleteness is typically higher at faint magnitudes as well as in the outer regions that are dominated by the most ancient and metal-poor stars. Due
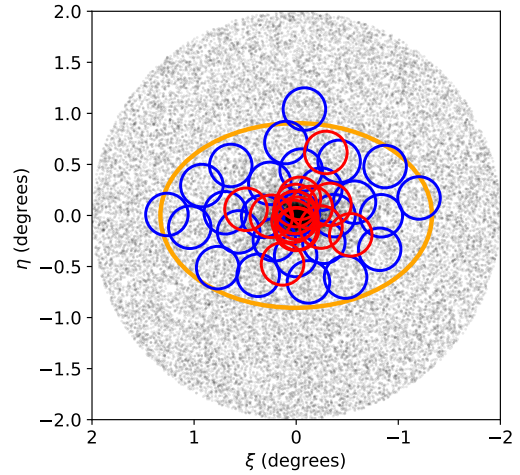

Fig. 1. *Gaia* DR3 catalogue (black dots) within 2° of the centre of the Sculptor dSph, consisting of 36 185 objects that possess photometry, proper motion, and parallax measurements. Positions of the 44 available VLT/FLAMES LR8 fields (~25′ diameter), many of which overlap, are shown with circles. In blue are the 27 previously analysed fields, and in red the 17 new fields. The nominal tidal radius of Sculptor (from Irwin & Hatzidimitriou 1995) is shown as an orange ellipse.

to the metallicity gradient in Sculptor, it is not possible to simply to correct for the incompleteness in the outer regions using the results from the inner (e.g. Romano & Starkenburg 2013). A complete and unbiased set of measurements of the [Fe/H] and v_{los} distributions over the entire RGB age range in Sculptor is needed to accurately constrain both the buildup of metals as a result of extended star formation and the loss of metals due to stellar feedback (e.g. Dekel & Silk 1986; Gilmore & Wyse 1991; Ferrara & Tolstoy 2000; Lanfranchi & Matteucci 2004; Fenner et al. 2006; Marcolini et al. 2008; Salvadori & Ferrara 2009; Revaz et al. 2009; Revaz & Jablonka 2018). A large and complete sample of RGB stars is also important because the quantification of scatter in the properties of individual stars is critical for a correct understanding of galactic-scale dynamics (e.g. Battaglia et al. 2013) and chemical evolution (e.g. Cayrel et al. 2004).

A long-standing challenge for this kind of study has been the accurate determination of the membership of individual stars (e.g. Battaglia & Starkenburg 2012). The *Gaia* proper motions and parallaxes are relatively new, first provided in *Gaia* Data Release (DR) 2 (Gaia Collaboration 2018a), and are regularly being improved, most recently in *Gaia* DR3 (Gaia Collaboration 2021). This highly accurate astrometry, which uses detailed, high-precision measurements of individual stars, provides unique insights into the global properties of nearby resolved galaxies (e.g. Gaia Collaboration 2018b; McConnachie & Venn 2020; Battaglia et al. 2022). Thus we take the opportunity to re-examine the Very Large Telescope (VLT) Fibre Large Array Multi Element Spectrograph (FLAMES) Ca II triplet (CaT) surveys that cover the whole area of the Sculptor dSph on the sky (see Fig. 1) and combine them with the *Gaia* DR3 catalogue to create a uniquely detailed and complete catalogue. Including both new and reprocessed archival VLT/FLAMES data, we present the most complete and homogeneous survey of the 3D velocities and metallicities of the resolved stellar population in any galaxy to date, enhancing Sculptor as a benchmark system for understanding galaxy formation and evolution on small scales.

2. VLT/FLAMES spectroscopy

The European Southern Observatory (ESO) VLT FLAMES spectrograph in GIRAFFE mode using the LR8 grating has provided spectra of RGB stars in the Sculptor dSph galaxy over nearly 20 years. Here we present extensive recent observations together with consistently analysed older programmes. All observations, recent and from the distant past, have been processed uniformly with the most up to date pipeline and additional software to give self-consistent velocities and metallicities, with accompanying errors, across all VLT/FLAMES LR8 datasets.

2.1. VLT/FLAMES LR8 observations

We extracted all spectra of individual stars in the direction of the Sculptor dSph galaxy from the ESO VLT archive observed with the FLAMES/GIRAFFE LR8 grating, covering the CaT spectral region ($\lambda\lambda 8498$, 8542, 8662 Å). This includes 67 independent observations from 10 different observation programmes[1], taken between 2003 and 2018 (see Table A.1), of 44 different pointings, 17 of which are new (see Fig. 1). All the observations from 2007 and earlier have been previously presented (e.g. Tolstoy et al. 2004; Battaglia et al. 2008a,b; Starkenburg et al. 2010) and have also provided the basis of searches for extremely metal-poor stars in Sculptor (e.g. Tafelmeyer et al. 2010; Starkenburg et al. 2013; Jablonka et al. 2015). The VLT/FLAMES LR8 observations are predominantly concentrated in the central region of the Sculptor dSph, where most of the stars are to be found. It also extends out to the nominal tidal radius (see Fig. 1), as defined by Irwin & Hatzidimitriou (1995). Irwin & Hatzidimitriou determined the tidal radius by fitting a King profile to the number density surface profile of stars along the los to Sculptor, taking into account the presence of Galactic foreground/background. The ellipticity was found to be $e = 0.32 \pm 0.03$ and the position angle PA $= 99 \pm 1$ deg.

The large collection of new VLT/FLAMES LR8 observations also includes repeat observations monitoring the same targets in the central field. Upcoming work (Arroyo Polonio et al., in prep.) will use these data for a full analysis of the properties of binary stars in the Sculptor dSph.

2.2. Processing the VLT/FLAMES LR8 spectra

The first step in producing a uniform catalogue of $v_{\rm los}$ and [Fe/H] measurements for RGB stars is to (re-)process all the available VLT/FLAMES LR8 observations with the most recent ESO pipeline (via the esoreflex tool; Freudling et al. 2013), including cosmic ray removal, heliocentric correction, and error arrays for each extracted spectrum. This results in 4646 individual spectra, of which 2257 are new (numbers per pointing are given in Table A.1). The total number includes multiple measurements of the same stars, and also Galactic foreground stars and spectra with too low signal-to-noise ratio ($S/N < 7$) to be consistently reliable. These are all removed from further analysis, as described in Sect. 3

The ESO VLT/FLAMES data reduction pipeline provides calibrated spectra with the instrumental effects removed, as well as new statistical error arrays for each extracted spectrum, which

were not available when the older data were analysed in 2008. These are the standard deviation of the re-sampled fluxes for each wavelength bin. The additional processing steps, still required after the ESO pipeline, are carried out using software developed over many years by Mike Irwin. An earlier version of this software was described in Battaglia et al. (2008b). The software used here has been adapted to make use of the error arrays provided by the ESO pipeline. This improves the reliability of the error determinations on the $v_{\rm los}$ and [Fe/H] measurements. Individual Fortran programmes are used, starting with adding accurate, well calibrated *Gaia* DR3 photometry converted to V magnitude (Riello et al. 2021), for each observed star into the fibre fits tables of the pipeline output. This photometry is later used to ensure uniform results in determining the CaT metallicities. All stars observed with VLT/FLAMES are found in the *Gaia* catalogue except one (AS5360[2]), which is in the *Gaia* DR3 photometric catalogue, but it lacks astrometric measurements. This single star, although it is a likely member based on the VLT/FLAMES spectroscopy, was removed from further consideration.

Before sky subtraction a simple check was made for each VLT/FLAMES field that the ESO pipeline wavelength calibration, which uses the internal arcs taken in daytime, matches the known positions of the numerous sky lines in the LR8 wavelength range. A global shift was then applied to all the spectra for each individual field to put all the fields on the same zero point. These shifts typically varied between 1 and $2.5\,{\rm km\,s^{-1}}$, but there were also a few observations with larger shifts. These shifts are listed in Table A.1. When the velocity shifts become large this is most likely due to a problem with the guide star positioning in setting up the observation or the available day-time calibration frames. This global check is carried out to ensure that there are no systematic offsets in velocity between different VLT/FLAMES pointings. The individual spectra once corrected for these small velocity shifts were then sky subtracted, again using the dedicated software from Mike Irwin. The sample of 4646 spectra was then ready to be analysed to determine membership and spectroscopic $v_{\rm los}$ and [Fe/H].

In Fig. 2 we show the effects of S/N on VLT/FLAMES LR8 spectra for stars with the same [Fe/H], demonstrating how sky subtraction becomes more challenging at lower S/N. Figure 3 shows on the same scale as Fig. 2 the strength of the sky lines compared to the CaT lines and the proximity of the strong sky lines. The dependence of the CaT line strength on metallicity is complex due to the variety of stellar atmospheric parameters ($T_{\rm eff}$, $\log g$), as is most clearly illustrated in Fig. 1 of Starkenburg et al. (2017). We show three spectra from our VLT/FLAMES LR8 sample with varying metallicity in Fig. 4. It is clear that the wings of the lines change most going from high to low [Fe/H]. This also means that, especially at low S/N the higher metallicity stars are more affected by nearby sky lines as the CaT wings will tend to overlap with the sky line residuals. We try to remove as many spurious measurements coming from sky subtraction problems as we can unambiguously identify, even though they are few and have a very limited effect on the final results.

As the majority of the spectra available were taken before *Gaia* was launched, our early observations contain a significant number of non-members. This results in independent samples of velocities and proper motion selections, which allows more wide-ranging checks on the membership boundaries than might otherwise have been possible. From 2018 onwards we were able to make use of a priori information from the *Gaia* DR2 proper

---

[1] 171.B-0588 PI: Tolstoy (DART LP); 072.D-0245 PI: Hill (FLAMES GTO); 076.B-0391 PI: Battaglia; 079.B-0435 PI: Battaglia; 593.D-0309 PI: Battaglia; 098.D-0160 PI: de Boer; 0100.B-0337 PI: Tolstoy; 0101.D-0210 PI: Skúladóttir; 0101.B-0189 PI: Tolstoy; 0102.B-0786 PI: Tolstoy.

[2] *Gaia* DR3 ID: 5003198370796137728; RA: 00 59 48.55; Dec: −33 48 14; $G \sim 19.77$. From VLT/FLAMES: $v_{\rm los} = 123\,{\rm km\,s^{-1}}$; [Fe/H] ~ -1.4.

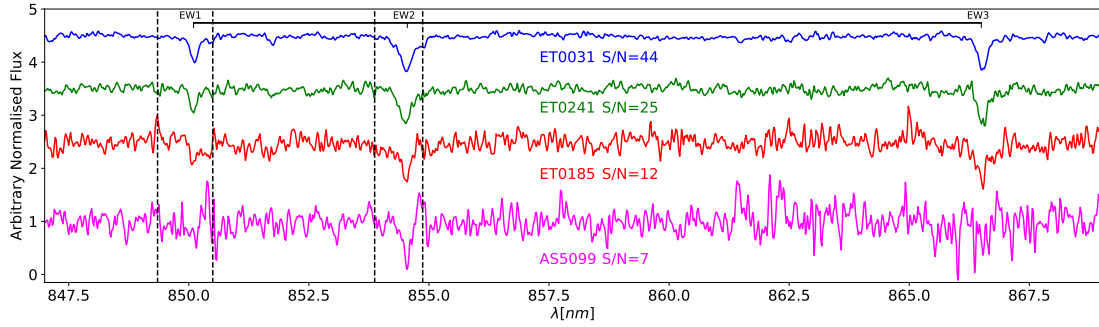**Fig. 2.** Normalised spectra of four RGB stars in the Sculptor dSph galaxy, all with [Fe/H] ∼ −1.7, for a range of S/N. The three CaT absorption lines for stars in the Sculptor dSph are marked at $\lambda\lambda 8500$ Å(EW1), 8545 Å(EW2), and 8665 Å(EW3). Vertical dashed black lines show the central positions of strong sky lines that can cause problematic residuals in low S/N spectra.
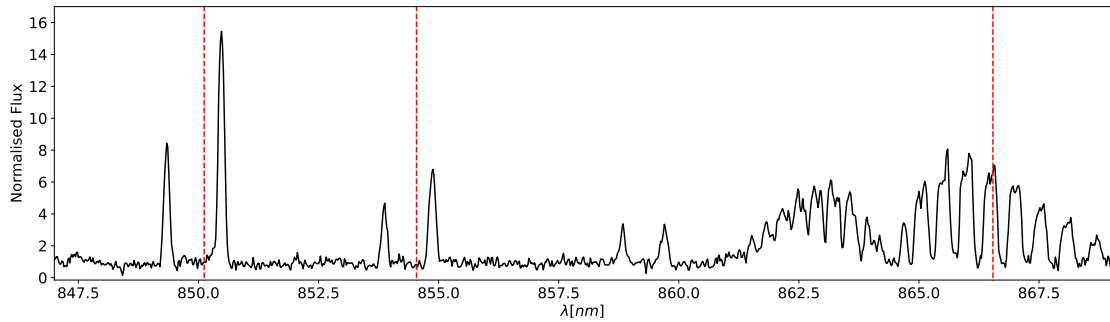

Fig. 3. Normalised sky spectrum from a single sky fibre, from the same observation and with the same normalisation as the top three spectra in Fig. 2. The central positions of the three CaT absorption lines at the mean velocity of the Sculptor dSph are marked as dashed red lines.
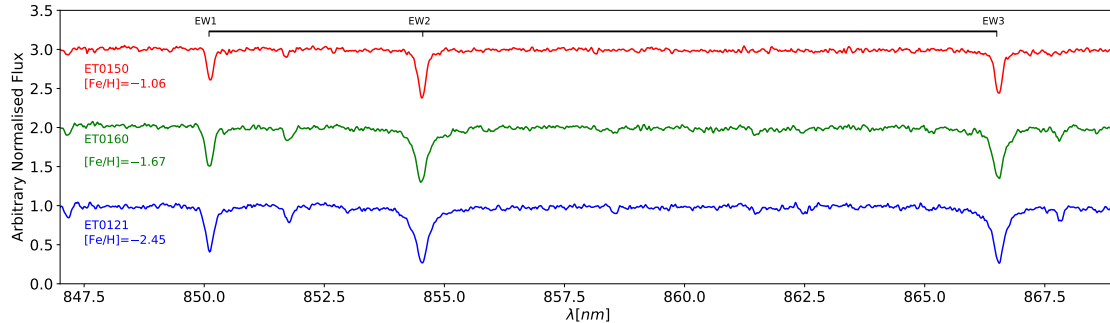

Fig. 4. Normalised high S/N (∼65−75) spectra of three RGB stars in the Sculptor dSph galaxy, with a range of metallicities, [Fe/H]. The three CaT absorption lines are marked.

motion catalogue, and as can be seen in Table A.1, this dramatically increased the efficiency at picking out likely members of the Sculptor dSph for spectroscopic follow-up. The multiple observations were used to test our error analysis more completely than has been possible in the past (e.g. Battaglia et al. 2008b, and see our Appendix B).

2.3. Measuring velocities (v_{los}) and metallicities ([Fe/H]) from VLT/FLAMES LR8 spectra

There has been extensive use of a variety of methods to determine the likely membership of stars in the Sculptor dSph: according to the spatial distribution (e.g. Demers et al. 1980), the colour-magnitude diagram (CMD) distribution (e.g. Da Costa 1984) and los velocities (e.g. Armandroff & Da Costa 1986; Aaronson & Olszewski 1987; Queloz et al. 1995) and more recently a combination of all of these, building up to the present day inclusion of parallax and proper motion from *Gaia* (e.g.

Battaglia et al. 2022). There has also been extensive use of metallicity indicators in low resolution spectra ($R < 8000$), such as the CaT (e.g. Tolstoy et al. 2001, 2004; Battaglia et al. 2008b; Starkenburg et al. 2010; Carrera et al. 2013), and the Mg triplet (e.g. Walker et al. 2009) to determine [Fe/H] and using Ca H&K lines as well as photometry (Chiti et al. 2018) and a broad spectral range (Kirby et al. 2010). Metallicities (and additional lines in the low resolution spectra) have also be used to refine membership determination of the stars in the Sculptor dSph (e.g. Battaglia & Starkenburg 2012).

2.3.1. The line-of-sight velocities (v_{los})

The los velocities[3], v_{los}, were determined from the VLT/FLAMES spectra using the three CaT lines (Figs. 2 and 4). In our processing we explored three different methods:

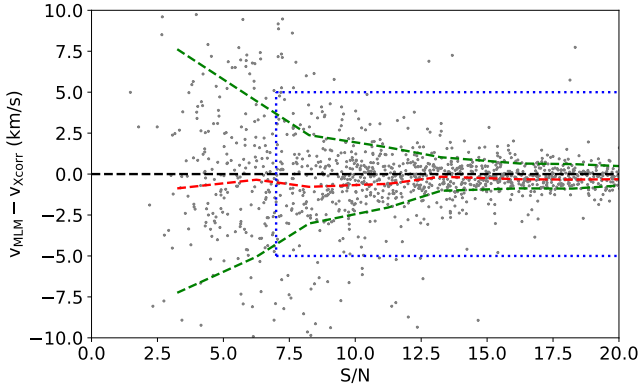[3] The los velocities are always in the heliocentric system.

Fig. 5. Differences in v_{los} at $S/N < 20$, as measured with the maximum likelihood (v_{MLM}) and the cross-correlation (v_{Xcorr}) methods on the same individual spectra, selected to have v_{los} in the range expected for Sculptor stars ($70{-}150\,\text{km s}^{-1}$). Dashed green lines are the mean values above and below zero (dashed black line), and the dashed red line is the mean of all velocity differences. The vertical dotted blue line shows the minimum acceptable $S/N = 7$, and the horizontal dotted blue lines show the limits for outliers, at $\pm 5\,\text{km s}^{-1}$.

(1) a fit of the individual lines; (2) cross correlation; and (3) the maximum likelihood method (MLM). All three methods used a template RGB spectrum for comparison. All methods should (and did) produce very similar results; however, MLM was the most statistically robust, once the ESO pipeline error arrays were utilised, and it could provide reliable error estimates. Significant differences in velocities determined for the same spectra with different methods ($\geq 5\,\text{km s}^{-1}$) were used to flag and remove (the few) clearly unreliable measurements at low S/N. This mismatch was typically created by poor sky subtraction at low S/N ($\lesssim 20$) where the presence of sky subtraction residuals created significant variations between different methods due to the proximity of strong sky lines to the CaT lines (Figs. 2 and 3). This effect can clearly be seen in the two lowest S/N spectra in Fig. 2. We tested the error determination using the sequence of repeated observations of the same stars (see Appendix B) for a subset of 96 stars from a monitoring programme looking for binary stars in Sculptor (Arroyo Polonio et al., in prep.). It was immediately apparent that the S/N varies for the same stars over the programme and between observations (see Fig. B.1). This was most likely due to differences in fibre positioning between different acquisitions of the same field. There were also a few obviously spurious measurements that are likely due to imperfections in the spectra (e.g. problems with sky subtraction or continuum definition) that can lead to errors in the results.

Two different methods of velocity measurements, MLM and cross-correlation, are compared in Fig. 5, for individual velocity measurements in the likely v_{los} membership range 70–150 km s^{-1}. The intrinsic scatter is expected to be $\lesssim 1\,\text{km s}^{-1}$, depending upon the S/N (see Fig. B.2). It can be seen that although there is scatter, the majority of measurements lie in the expected range, and the scatter increases as the S/N decreases. In Fig. 6 we can see how the MLM errors increased as the S/N decreased with a similar spread to that seen in Fig. 5, in both cases the scatter appears to expand significantly for $S/N \lesssim 7$. Both the difference in MLM and Xcorr velocities and the MLM errors on velocity measurements were used as cuts for reliable v_{los} measurements. The small number of stars at all S/N where the two velocity measurements differ well beyond their errors (see Fig. 5) were usually problems with the spectrum, for example, a poorly subtracted cosmic ray or sky line. This was quite
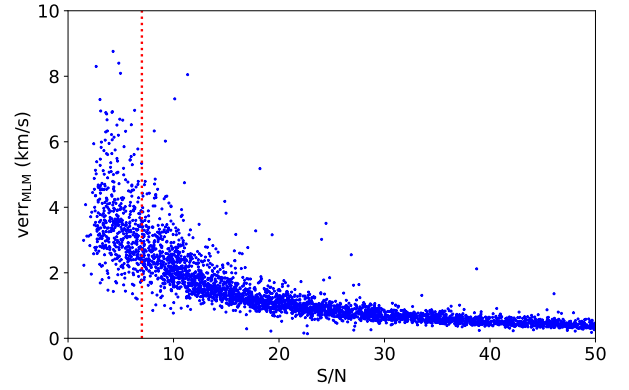

Fig. 6. MLM velocity errors as a function of S/N for the full sample of individual VLT/FLAMES LR8 spectra, selected to have v_{los} in the expected range for Sculptor stars ($70{-}150\,\text{km s}^{-1}$). The dashed red line indicates where the $S/N > 7$ cut, which is applied to the final selection, falls.

a rare occurrence ($\sim$200 measurements out of 4646) and thus it was decided to neglect those spectra with a large difference ($>5\,\text{km s}^{-1}$, which is $\sim 3\sigma$) between the different velocity determinations. On some rare occasions a distant background object like a compact galaxy or an active galactic nucleus (AGN) found its way into the sample, these were sometimes also identifiable in this way. Figure 5 suggests that the measurements remain reliable until $S/N \approx 7$ (vertical blue dotted line), even if the uncertainties are increasing. This was also consistent with what is seen in the MLM error distribution against S/N in Fig. 6. After adopting the cuts $S/N > 7$ and $|v_{\text{MLM}} - v_{\text{Xcorr}}| < 5\,\text{km s}^{-1}$, for the individual spectra, there were a total of 3312 VLT/FLAMES spectra for 1701 individual stars with reliable v_{los}, within the likely membership range of the Sculptor dSph galaxy ($70{-}150\,\text{km s}^{-1}$).

The v_{los} measurements for two or more individual spectra with $S/N > 7$ for the same star were combined, and weighted by $1/v_{\text{err}}^2$. The mean measurements and their uncertainties are presented for stars with multiple measurements, as the mean and standard deviation of this combination. The cases of only a single measurement have a zero in the variance column. There are a significant number of stars in the whole VLT/FLAMES LR8 sample of 4646 spectra where the spectroscopic v_{los} are clearly inconsistent with membership in the Sculptor dSph, for example $v_{\text{los}} \gg 150\,\text{km s}^{-1}$ or $v_{\text{los}} \ll 70\,\text{km s}^{-1}$. Before *Gaia* only the position of the RGB in Sculptor could be used to select targets for spectroscopic follow-up, resulting in quite large numbers of non-members, especially in the outer regions. These non-members and their basic properties are recorded in Table E.2 available at the CDS.

2.3.2. The spectroscopic equivalent widths

Assuming that the target is an RGB member of the Sculptor dSph, then the equivalent widths (EWs) of the strongest two CaT lines, EW2 and EW3 at $\lambda\lambda 8542\,\text{Å}$ & $\lambda\lambda 8662\,\text{Å}$ (see Fig. 4), can be used to determine [Fe/H], through the well-established formalism (e.g. Starkenburg et al. 2010, and references therein). The EWs of all three lines, EW1, EW2, and EW3, were measured using two methods: (1) integrating over the CaT lines; and (2) a more sophisticated fitting of both lines, assuming Gaussian profiles. In fitting the EWs the code computes a linear scale factor that best maps the Gaussian EWs onto the direct integration EWs and then applies that scale factor to the Gaussian EWs.
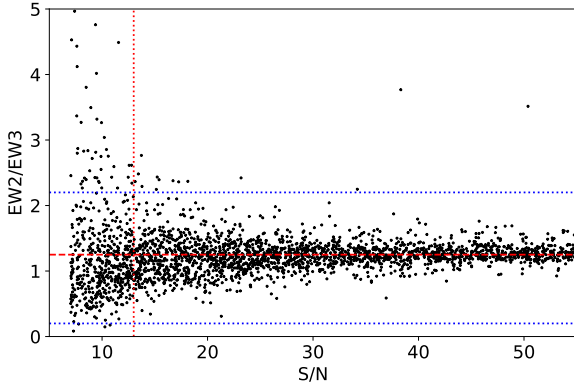
Fig. 7. Ratios of the two strongest CaT lines (EW2/EW3) as a function of S/N. The vertical dotted red line is at $S/N = 13$, and dotted blue lines are limits of the reasonable values of the ratio at $0.2 < EW2/EW3 < 2.2$. Outside this range there is most likely a problem with a poorly subtracted sky line interfering with the measurement of EW2 and/or EW3.

This effectively corrected for the difference between the real data where the CaT lines have (non-Gaussian) wings that depend on metallicity and a Gaussian model (Battaglia et al. 2008b). The two approaches gave comparable results, but the fitting method provided more robust measurements, so this is what is presented here. All three lines were used for quality analysis of the spectrum, as peculiar ratios (e.g. EW1/EW2 and EW2/EW3) provide evidence for sky subtraction problems (see Fig. 7).

We looked through spectra at low S/N and also at cases with unusual [Fe/H] values, and determined that the S/N at which reliable metallicities can be obtained was somewhat higher than is required to measure reliable v_{los}. Hence we adopted more severe cuts to our sample of spectra, $S/N > 13$, to obtain reliable [Fe/H] measurements. The measured EW ratios of different CaT lines were compared to their expected ratios, to ensure that individual lines were being measured accurately. This check flagged stars, mostly with low S/N, whose measurements had intrinsically large uncertainties often with clear sky subtraction residuals (see the lowest S/N stars in Fig. 2). In addition, there were cases where an unfortunately located cosmic ray led to problems with the sky subtraction, and/or an incorrect identification of the CaT lines. Thus, stars with strongly divergent EW1/EW2 or EW2/EW3 (see Fig. 7) ratios were removed, as were stars with unusually large EW2 or EW3 values, well beyond those expected. We were careful to ensure that the limits did not remove any realistic but unexpected measurements. This gave us a sample of 1414 stars with reliable [Fe/H] measurements, assuming the stars are members of Sculptor dSph, which will be determined in Sect. 3.

As with the velocities (Sect. 2.3.1), we combined the multiple measurements of [Fe/H] determined from EWs from independent spectra for the same stars, where the mean is weighted by the S/N. The errors on the [Fe/H] came from assuming that the intrinsic error on the sum of the two strongest lines (EW2+EW3) is 6/(S/N), where the constant is determined from comparing repeat measurements, and then this error was put into the metallicity equation with these limits added and subtracted for each measurement to obtain the error on the [Fe/H] determination (Battaglia et al. 2008b; Starkenburg et al. 2010). The mean measurements and their uncertainties are presented as a single value for stars with multiple measurements, as the mean and standard deviation of this combination. The cases of only a single measurement have zero in the variance column.

A sub-sample of our LR8 measurements also had VLT VLT/FLAMES High Resolution (HR, $R \sim 20\,000$) abundance analysis (Hill et al. 2019). These HR observations allowed direct measurements of numerous Fe I and Fe II lines and thus provided a good check of our metallicity calibration (see Appendix C). In addition, they provided abundances for a number of other elements, including Ca. From this comparison we see a possible, small, offset in the measurements of the two different works, such that the [Fe/H] from VLT/FLAMES LR8 are ~0.1 dex more metal-rich than that measured by VLT/FLAMES HR10 (see Fig. C.1). There is no obvious bias at play, there are no trends in the offset with metallicity, [Ca/H], or the G magnitudes of the stars (see Fig. C.2). The [Ca/H] has a well defined trend with [Fe/H] in Sculptor (e.g. Hill et al. 2019; Shetrone et al. 2003), so if this were the issue we would expect a different slope in Fig. C.1a. The scatter is within the uncertainties expected from the errors, and for two different methods, differently calibrated, such minor systematic offsets are not unexpected.

2.3.3. Other surveys

There have been several other major low/medium-resolution spectroscopic surveys of the Sculptor dSph made with other telescopes. For example, the Michigan/MIKE Fiber Spectrograph (MMFS) at the *Magellan* observatory was used to make a survey of 1365 likely members observed in the Mg-triplet spectral range (Walker et al. 2009), and 262 of these have not been observed by VLT/FLAMES. In addition, there has been a Keck DEep Imaging Multi-Object Spectrograph (DEIMOS) study of 388 stars over a wide wavelength range using all the information in the faint lines (Kirby et al. 2009). There are nine stars in the Keck sample that are neither in the Walker et al. sample nor in our VLT/FLAMES sample. These missing stars are typically fainter stars in the central region of the Sculptor dSph. Undoubtedly, new more complete samples will become available in the near future when 4MOST starts operation (e.g. the 4DWARFS survey, PI: Á. Skúladóttir, and the 4MOST low-resolution halo survey, PIs: E. Starkenburg & C. Worley). The Subaru Prime Focus Spectrograph survey will also include Sculptor. The work presented in this paper should be useful for future surveys, using the overlapping observations to test calibration, and serve as a baseline for future galaxy-wide studies of the properties of variability and binary systems in Sculptor.

3. Membership selection

The *Gaia* DR3 catalogue provides uniquely accurate information on the motions of stars in the plane of the sky. Even at the distance of the Sculptor dSph, the *Gaia* astrometry makes it possible to distinguish Galactic stars from Sculptor members. For individual stars we have parallax measurements with detailed error analysis; exquisitely accurate photometry, which gives the position of a star in a CMD; proper motions in right ascension (RA) and declination (Dec.) and their errors. The combination of all this information is a powerful discriminator for membership of a star in the Sculptor dSph. Not invoking too much prior information allows an unbiased assessment to be made of where the limits of membership lie. This is especially important in the outer regions of Sculptor.

We describe here how stars belonging to the Sculptor population were selected on the basis of their *Gaia* DR3 proper motions and parallaxes, and the los velocities measured with
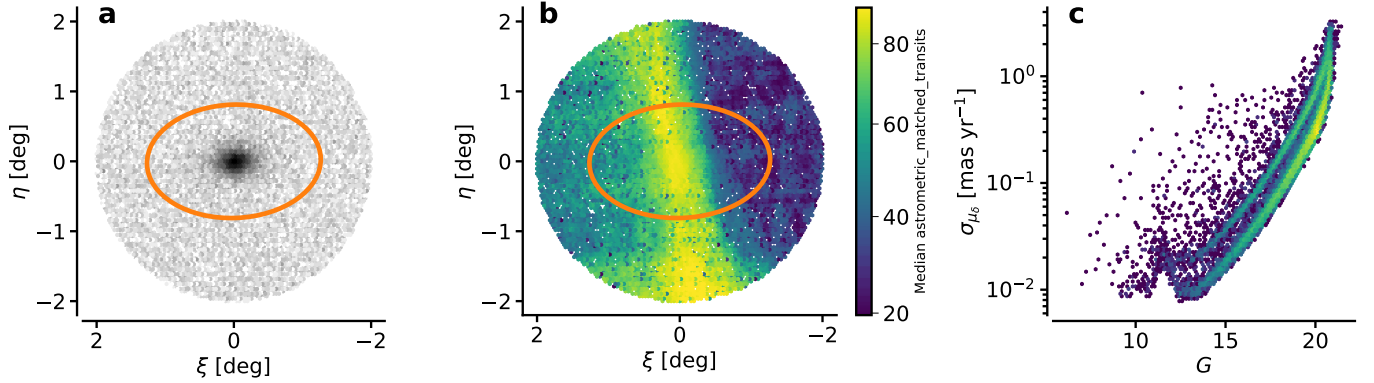
Fig. 8. *Gaia* DR3 data within two degrees of the centre of Sculptor. (a) Distribution of sources on the sky. (b) Median number of astrometric observations (`astrometric_matched_transits`) matched to a given source. (c) Uncertainty on μ_δ as a function of G. The sequence at higher values corresponds to the area in panel (b) with fewer visits. The orange ellipse in panels (a) and (b) indicates the nominal tidal radius of Sculptor.

VLT/FLAMES. The membership selection code is available on GitHub[4].

3.1. Gaia DR3 data in the Sculptor field

All *Gaia* DR3 sources in the Sculptor field that have parallaxes, proper motions, and $(G_{BP} - G_{RP})$ colours were selected according to the query listed in Appendix D. Figure 8 shows the distribution of these sources on the sky and the median number of astrometric measurements per source (`astrometric_matched_transits`). Figure 8b shows that Sculptor is located in a region of the sky with a rather uneven distribution in the number of observations collected per source. The core of Sculptor is very well observed, but the area west of Sculptor is less well covered. This leads to the difference in proper motion errors illustrated Fig. 8c, which shows the uncertainty on the proper motion in Dec. versus G-band magnitude. The sequence at larger values of the uncertainties corresponds to the less well observed sky area west of Sculptor. A similar effect is seen in the RA proper motion uncertainties. The parallax uncertainties show no such split. However, this dichotomy in the uncertainties has no negative effect on the selection of Sculptor members.

A first exploratory analysis of the sources in the direction of Sculptor dSph was carried out by examining their distribution on the sky, in parallax, in the CMD and in the normalised corrected flux excess factor $|C^*/\sigma_{C^*}|$, as defined by Riello et al. (2021). High values of $|C^*/\sigma_{C^*}|$ can indicate crowding issues or the presence of (extended) non-stellar sources. A large fraction of sources at high values of $|C^*/\sigma_{C^*}|$ were found to be listed as quasi-stellar objects (QSOs) or galaxy candidates in the *Gaia* DR3 catalogue, thus indicating that source crowding is not a major concern in the Sculptor field. This is confirmed by the value of the M_{10} indicator (Cantat-Gaudin et al. 2023), which is 21.2 for the Sculptor field, indicating a high completeness of the *Gaia* DR3 catalogue out to the *Gaia* survey limit at $G \sim 21$ and a corresponding lack of crowding issues.

A preliminary selection of Sculptor stars was made on the basis of their proper motions and parallaxes, with the latter corrected for the parallax bias using the recipe from Lindegren et al. (2021). The results show that the mean parallax bias correction applied to the selected Sculptor stars was ~17 μas cor-

responding to the mean parallax bias for QSOs in *Gaia* DR3 (Lindegren et al. 2021). However, the mean parallax of the *Gaia* celestial reference frame objects (QSOs and AGNs) from *Gaia* DR3 (Gaia Collaboration 2022) in the Sculptor field is −39 μas, suggesting that a larger correction should be applied. In addition, the raw parallaxes of the preliminary list of members have a median value of 13.6 μas, very close to the nominal Sculptor parallax 11.9 ± 0.2 μas, based on the distance modules listed in Battaglia et al. (2022)[5]. We therefore decided to work with the raw parallaxes and ignore the bias corrections.

To select Sculptor member stars, we assumed the proper motion and the parallax corresponding to the distance listed in (see our Table 1 Battaglia et al. 2022) and calculated a membership score, z_i, for each *Gaia* DR3 source, i, in the Sculptor field:

$$z_i = \mathbf{v}_i'(\mathbf{C}_i + \mathbf{D})^{-1}\mathbf{v}_i, \tag{1}$$

where $'$ indicates the transpose of the vector, $\mathbf{v}_i$:

$$\mathbf{v}_i = \begin{pmatrix} \varpi_i - \langle\varpi\rangle_{scl} \\ \mu_{\alpha*,i} - \langle\mu_{\alpha*}\rangle_{scl} \\ \mu_{\delta,i} - \langle\mu_\delta\rangle_{scl} \end{pmatrix}. \tag{2}$$

The matrix $\mathbf{C}_i$ is the covariance matrix for the parallax and proper motions of source i as listed in *Gaia* DR3. The matrix $\mathbf{D}$ contains the squares of the uncertainties on the mean parallax and proper motions of Sculptor on its diagonal and all other elements are zero.

The membership score z should be a χ^2 distribution with three degrees of freedom for Sculptor members, and an upper limit on z can be used to select members. Figure 9a shows a histogram of z_i that reveals a clear presence of two distinct groups of sources, at low (Sculptor members) and high (non-members) values of z; the orange line shows the value $z_{lim} = 14.2$, which is the limit for a χ^2_3 distribution corresponding to a 3σ limit for a 1D normal distribution. Figure 9b shows that for $z < z_{lim}$ the source parallaxes are normally distributed around the mean Sculptor parallax, while above the limit the distribution strongly deviates from normal. This can be explained as a population of sources at effectively zero parallax concentrated around the proper motion of Sculptor ($z < z_{lim}$) and a population of Milky

---

5 Applying either the 17 or 39 μas parallax correction would result in a distance modulus for Sculptor of 17.6 or 16.4, which are both clearly incompatible with the observed apparent brightness of the Sculptor horizontal branch at $G \approx 20.1$.
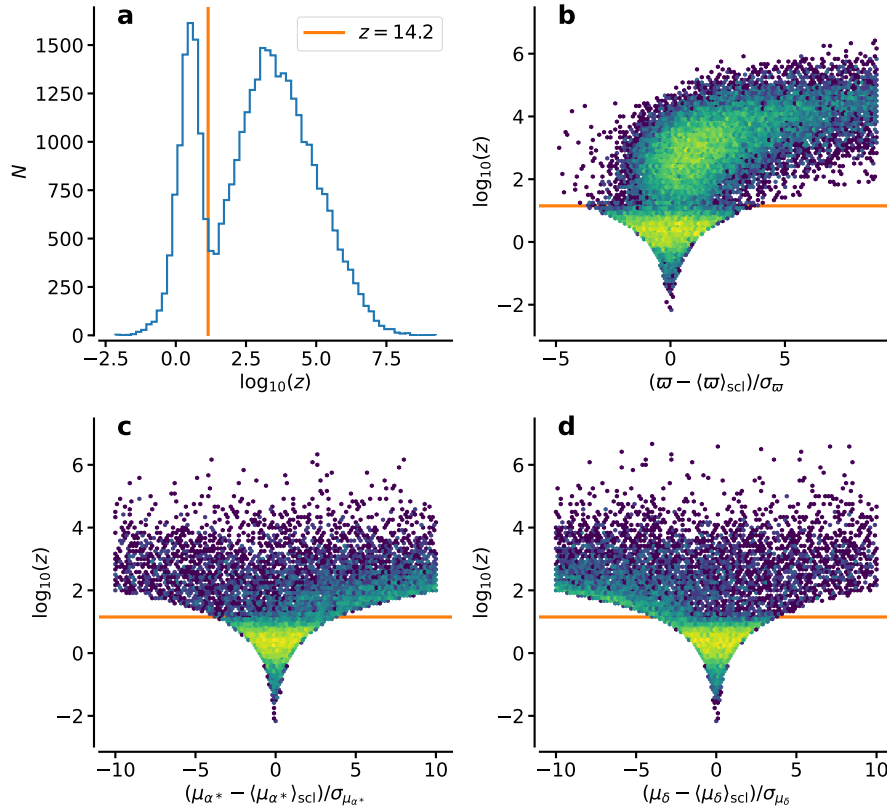
Fig. 9. Sculptor membership score, z. (a) Histogram of $\log_{10}(z)$ for all sources in the Sculptor field, where Sculptor members are expected to have $z < z_{\text{lim}} = 14.2$. The Distribution of $\log_{10}(z)$ is shown as a function of: (b) $(\varpi - \langle\varpi\rangle_{\text{scl}})/\sigma_{\varpi}$; (c) $(\mu_{\alpha*} - \langle\mu_{\alpha*}\rangle_{\text{scl}})/\sigma_{\mu_{\alpha*}}$; and (d) $(\mu_{\delta} - \langle\mu_{\delta}\rangle_{\text{scl}})/\sigma_{\mu_{\delta}}$. The orange line always indicates $z_{\text{lim}} = 14.2$, which is the equivalent of 3σ for a 1D normal distribution, or the 99.9% tile equivalent of the theoretical distribution of Sculptor members.

Way stars with different proper motions (leading to high values of $z > z_{\text{lim}}$) and significant positive parallaxes (stars at close distances). The sharp boundary suggests that foreground stars are effectively removed without introducing an explicit limit on the parallax ϖ or ϖ/σ_{ϖ}. Figures 9c, d show that in proper motions the boundary at $z_{\text{lim}} = 14.2$ is not as well defined, with a smooth transition of large positive $\mu_{\alpha*}$ values and large negative μ_{δ} values. This indicates the presence of interlopers belonging to the Milky Way stellar population.

3.2. Sculptor membership selection

Selecting Sculptor stars simply according to $z < 14.2$ results in 8861 members. We removed sources with $|C^*/\sigma_{C^*}| > 7$ and values of the re-normalised unit weight error (RUWE) parameter above 1.25. These high RUWE sources stand out as having much larger parallax errors than the mean for sources at similar brightness. These selections leave 8375 sources as Sculptor members. The distributions of the parallaxes and proper motions are consistent with 1D normal distributions, with a slight excess of negative μ_{δ} values (see Fig. 9b). The widths of the distributions suggest that the uncertainties on the parallaxes and proper motions in RA and Dec. are underestimated by 7, 12, and 14 percent, respectively, consistent with other findings in the literature (e.g. Table 1 in Fabricius et al. 2021). The median parallax is 0.0136 mas. The weighted mean proper motions are $\mu_{\alpha*} = 0.095 \pm 0.002$ and $\mu_{\delta} = -0.154 \pm 0.002$ mas yr^{-1}, with a correlation coefficient of -0.36 (like the parallaxes, the proper motions are not corrected for systematic errors). The distributions of the selected sources on the sky and in the CMD are

shown in Fig. 10. The CMD in Fig. 10c shows the stars outside the nominal tidal radius of Sculptor. This shows that our adopted definition of the tidal radius (Irwin & Hatzidimitriou 1995) is consistent with the *Gaia* selection as the outside population looks entirely consistent with foreground contamination. The distribution is representative of Milky Way stars in the direction of Sculptor as is confirmed by selecting stars on the same parallax and proper motion criteria in a control field 4 degrees to the east of Sculptor.

Next we selected Sculptor member stars from the VLT/FLAMES LR8 survey by also accounting for the los velocity, v_{los}. We used the above derived uncertainty inflation factors (1.07, 1.12, and 1.14 for parallax and proper motion in RA and Dec., respectively) and the weighted mean proper motions of Sculptor and their covariance matrix. We calculated the z value again according to Eq. (1) but with

$$\mathbf{v}_i = \begin{pmatrix} \varpi_i - \langle\varpi\rangle_{\text{scl}} \\ \mu_{\alpha*,i} - \langle\mu_{\alpha*}\rangle_{\text{scl}} \\ \mu_{\delta,i} - \langle\mu_{\delta}\rangle_{\text{scl}} \\ v_{\text{los},i} - \langle v_{\text{los}}\rangle_{\text{scl}} \end{pmatrix} \tag{3}$$

and

$$\mathbf{D} = \begin{pmatrix} \sigma^2_{\varpi,\text{scl}} & 0 & 0 \\ 0 & \mathbf{C}_{\mu,\text{scl}} & 0 \\ 0 & 0 & \sigma^2_{v_{\text{los,scl}}} + \sigma^2_{\text{scl}} \end{pmatrix}, \tag{4}$$

where $\mathbf{C}_{\mu,\text{scl}}$ is the covariance matrix of the mean proper motions for Sculptor (derived above) and σ_{scl} is the los velocity dispersion of Sculptor. We use $\langle v_{\text{los}}\rangle_{\text{scl}} = 110.6 \pm 0.5$ km s^{-1} and
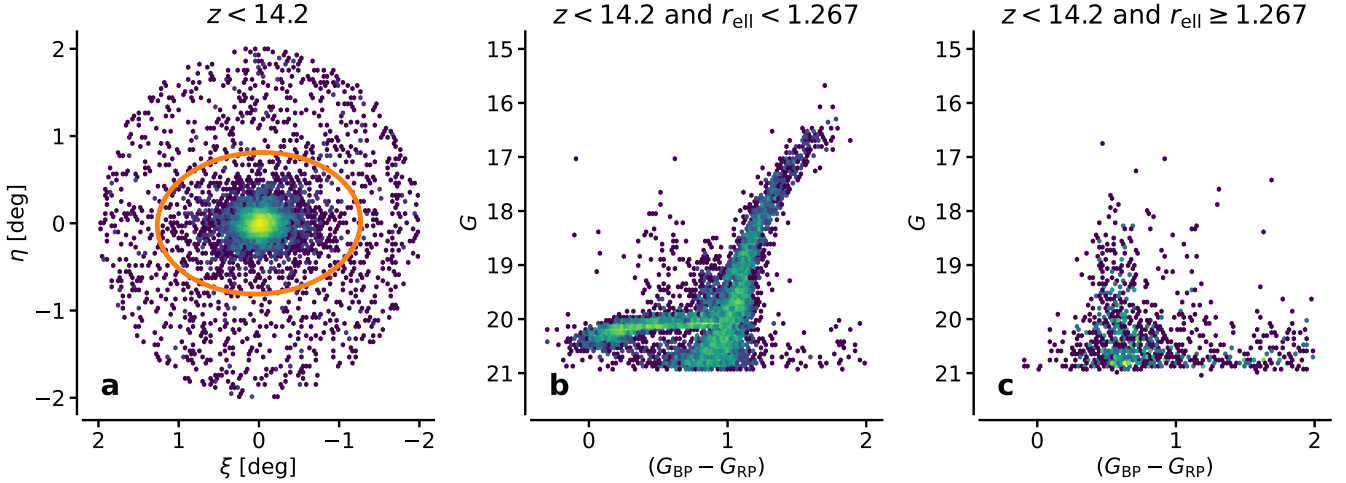
Fig. 10. Sculptor members selected on the basis of their parallaxes and proper motions. (a) Distribution on the sky. The orange ellipse indicates the nominal tidal radius of Sculptor. (b) and (c) CMDs for the Sculptor members located inside and outside the nominal tidal radius ($r_{\rm ell} = 1.267°$), respectively.

$\sigma_{\rm scl} = 10.10$ km s^{-1} (Battaglia et al. 2008a). The covariance matrices $\mathbf{C}_i$ include an additional diagonal term, corresponding to the uncertainty on the measured radial velocity for star i. The upper limit on z, $z_{\rm lim} = 16.3$, now follows from the χ^2_4 distribution. The membership selection results in 1604 out of 1701 stars selected as LR8 radial velocity members of Sculptor with an additional three stars as borderline cases. Thus, out of the Sculptor VLT/FLAMES LR8 spectroscopic $v_{\rm los}$ members (with velocities in the range 70–150 km s^{-1}), 94% are confirmed to be member stars when *Gaia* DR3 information is taken into account. There were no stars with velocities outside this range in our spectroscopic sample that had *Gaia* DR3 properties consistent with membership in Sculptor dSph. On the other hand, out of the 1609 stars in our spectroscopic sample that are members according to *Gaia* DR3 1604 or 99.7% are confirmed as Sculptor members once $v_{\rm los}$ is also included.

Figure 11 shows the z membership score as a function of the total proper motion, parallax, los velocity, and metallicity. It is clear from this figure that most of the 95 non-members from the VLT/FLAMES spectroscopic sample with 70 km s^{-1} > $v_{\rm los}$ < 150 km s^{-1} are stars with large proper motions (see Fig. 11a), clearly not belonging to the Sculptor dSph. The non-members do not stand out in los velocity (Fig. 11c) but do tend to be more metal-rich (Fig. 11d) and have larger parallaxes (Fig. 11b) than the bulk of the Sculptor members in the VLT/FLAMES sample. It is the combination of all these different measurements that make the most powerful membership determination. The three green circled orange symbols in all the panels of Fig. 11 indicate stars that are formally non-members (according to the z-score but in proper motion, arguably the most stringent criteria, combined with $v_{\rm los}$, are consistent with being Sculptor members and well separated from the other non-members. These three stars could thus be considered borderline cases and may well be members of Sculptor. Their *Gaia* properties and their spectroscopic properties are given in the results table (Table E.1) available at the CDS.

Figure 12 shows the distribution of the VLT/FLAMES members on the sky, in proper motion, and over the CMD, where the background colour coding indicates the density of Sculptor sources selected on the basis of their proper motion and parallax only. In Fig. 12 we also show where the borderline cases identified in Fig. 11 lie. They also show properties consistent with membership.

Figures 12a and b show how the members are concentrated in the central regions of the sky (by design in the VLT/FLAMES survey) and proper motion distributions for Sculptor. It is clear from Fig. 12a that the nominal tidal radius used (from Irwin & Hatzidimitriou 1995) is consistent with the confirmed member distribution in Sculptor. However, the spectroscopic follow-up did not extend much beyond this limit as there were very few likely members along the Sculptor RGB. In the northern-most VLT/FLAMES field (Scl025) there were spectra of 4 stars that passed the quality criteria and had radial velocities consistent with membership in Sculptor dSph, but only 1 of these also had proper motions and parallax consistent with membership (scl_25_031). This single star is only just beyond the nominal tidal radius, as can be seen in Fig. 12a. Larger fields of view, like that provided by 4MOST, will be best suited to search for extra-tidal stars (Skúladóttir et al. 2023).

In Figs. 12c and d, the CMDs show the location of the VLT/FLAMES members on the RGB. In both CMD panels the sources bluewards of the RGB at magnitudes between $G = 20$ and $G = 18.5$ are probably dominated by Milky Way interlopers (see Fig. 10). However, these (possible) interlopers are indistinguishable from Sculptor members within our current criteria. In addition, it can be seen that there are ~12 stars in Fig. 12c that lie to the red of the Sculptor RGB in ($G - G_{\rm RP}$), but they appear on the RGB in ($G_{\rm BP} - G_{\rm RP}$) in Fig. 12d. These are stars with a neighbour in *Gaia* DR3 within 3 arcsec, which can lead to blending of the $G_{\rm BP}$ and $G_{\rm RP}$ images of both sources and thus cross-talk between the integrated fluxes for these cases. This means that both $G_{\rm BP}$ and $G_{\rm RP}$ are biased, with an overestimated flux due to the neighbouring source. This also shows up in $G - G_{\rm BP}$ as too blue. In $G_{\rm BP} - G_{\rm RP}$ the biases compensate. We see no effect in the spectra, so either the 1.2 arcsec VLT/FLAMES fibres do not see the neighbouring object, or it is a sufficiently different source that does not affect our CaT spectra.

3.3. Comparing with previous membership determinations

Other groups have made membership selections for Sculptor based on *Gaia* DR2 and *Gaia* DR3 using different criteria (e.g. Simon 2018; McConnachie & Venn 2020; Battaglia et al. 2022), determining the probability of membership based upon the expectations of a Sculptor-like population in this region of
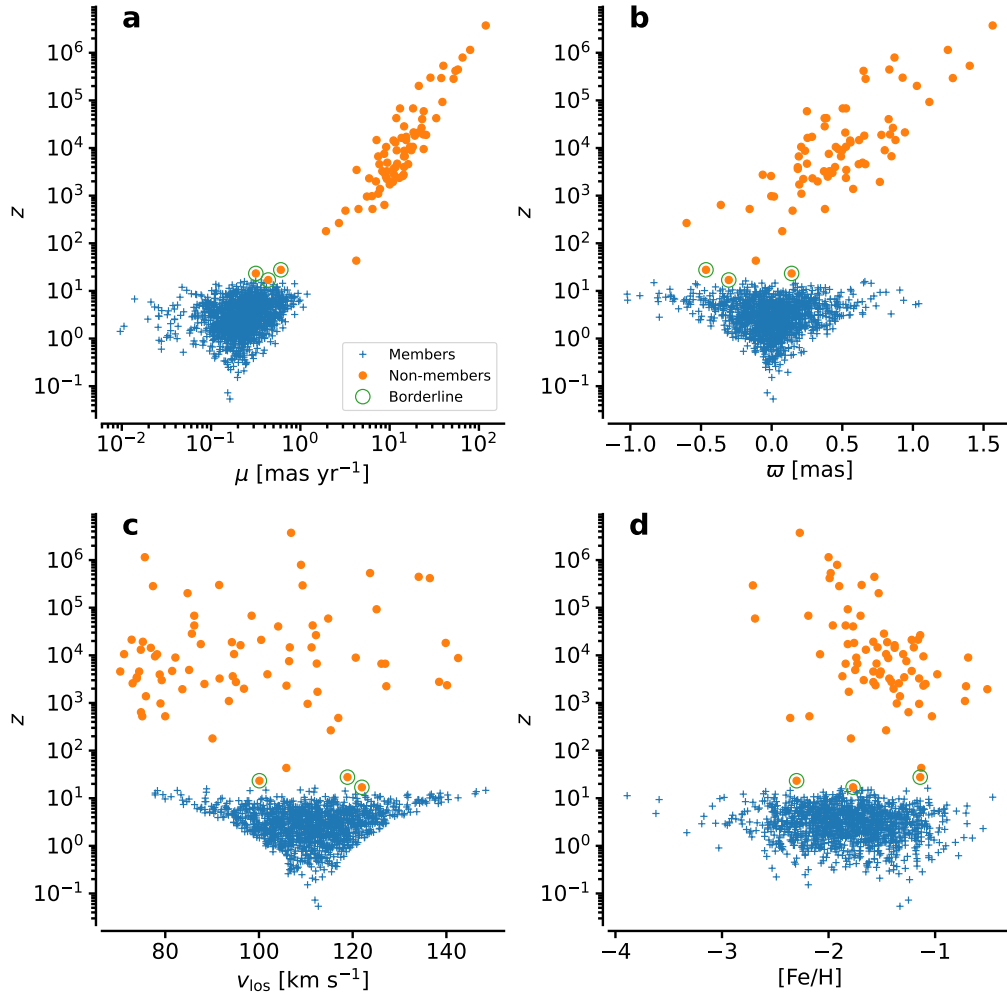
Fig. 11. z membership score of stars in the VLT/FLAMES LR8 sample as a function of: (a) total proper motion, μ; (b) parallax; (c) los velocity; and (d) metallicity (using only the 1339 reliable measurements). This shows the clean separation between Sculptor members and non-members. The three orange dots with green circles are borderline cases.

the sky. Typically these selections make assumptions, for example on the expected distribution in the sky and in the CMD that may potentially lead to small numbers of members being overlooked in sparsely populated regions. This is not critical for global studies to compare the properties of many different dwarf galaxies. Here, as we want to explore the Sculptor dwarf galaxy in detail, we preferred not to make any assumptions on either the spatial distribution of the stars nor their location in the CMD, so that we can look in detail at the selection and not rule out the presence of unusual members or possible members beyond the nominal tidal radius. There are slight differences between our *Gaia*-only selection of 8375 likely members and the 6576 sources that Battaglia et al. (2022) assigned a probability of membership, $P > 95\%$, but they are small enough not make any significant difference to the results. Of the 1604 members in our *Gaia* DR3-LR8 sample, 32 (mostly faint) stars are not in the Battaglia et al. catalogue of members. Some of these can be explained by the application of different quality cuts on the *Gaia* sources (e.g. AGN flags, duplicates). They are all on the RGB in the CMD and within the nominal tidal radius. There are 5 stars that both Battaglia et al. and our selection find to be likely *Gaia* members but they are VLT/FLAMES v_{los} non-members. These are therefore extremely small differences. Both methods are approaching the border between members and non-members

in slightly different ways and so small inconsistencies are not surprising.

3.4. Completeness of the Gaia DR3-LR8 survey

The spectroscopic follow-up covers the full width (and beyond) of the RGB (see Fig. 12d), as it was designed to do. It also populates well the physical centre of Sculptor on the sky, where most of the stars are to be found (Fig. 12a). We have 1701 VLT/FLAMES LR8 spectra with v_{los} broadly consistent with membership of the Sculptor dSph, 70–150 km s^{-1}, and $S/N > 7$. Out of these, 1604 have *Gaia* DR3 astrometry consistent with membership of the Sculptor dSph and 96 do not. In addition, there are three borderline stars that appear to be broadly consistent with Sculptor membership but formally do not make the cut in z. It is interesting to note that roughly 6% of previously identified velocity members are actually non-members when the *Gaia* astrometry is included. In the outer regions there are very few stars and so each one is important in determining the properties of the sparsely populated regions, and here it is critical that members and non-members are correctly separated.

In Fig. 13 we plot an overview of the completeness as a function of *Gaia* G-magnitude of the *Gaia* DR3-LR8 sample. We observed ~55% of the *Gaia* selection with VLT/FLAMES in
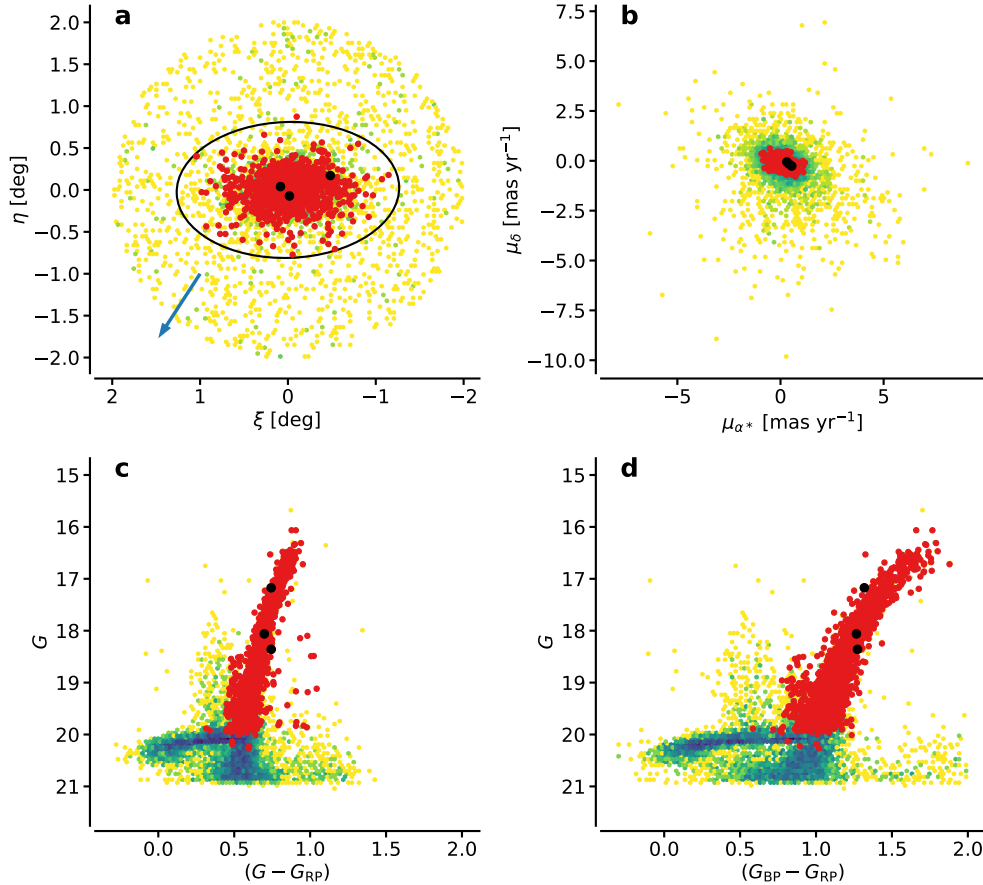
Fig. 12. Sculptor members in the VLT/FLAMES LR8 sample (red), as well as all *Gaia* DR3 Sculptor members selected on the basis of parallax and proper motion only (yellow-green colour coding): (a) on the sky, where the black ellipse indicates the nominal tidal radius and the blue arrow the direction of proper motion of Sculptor in the plane of the sky; (b) in proper motion; and (c) and (d) in the CMDs. The larger black symbols indicate the borderline cases between non-members and members identified in Fig. 11.

the range $G = 16$–20 mag, and with >70% completeness in the brightest range, $G < 18.75$. In Fig. 14 the same comparison is made as a function of elliptical radius. The completeness is quite uneven due to the decreasing numbers of stars going towards the outer sparse regions of Sculptor. The dip in the centre is due to the large numbers here and the difficulties in putting them all on to VLT/FLAMES fibres due to crowding. The completeness in the central, more metal-rich region of the galaxy is fairly similar in percentages to the outer, more metal-poor regions (see Fig. 14); however, in total numbers, the central region lacks spectroscopic observations of more stars.

4. Results

The Sculptor dSph is a very well-studied galaxy. Here we looked at a new combination of proper motions and spectroscopic velocities for 1604 individual RGB stars found over the full area of the galaxy on the sky, from the centre out to the nominal tidal radius (Fig. 12a). This combination provides a powerful method for accurately selecting Sculptor member stars, especially in the more challenging, sparse outer regions. This makes it useful to (re-)investigate the systemic velocity and other global properties on the basis of this new dataset (see Table 1). Furthermore, for a subset of 1339 Sculptor stars, whose spectra had $S/N > 13$, we also could provide reliable metallicities, [Fe/H]. The values of v_{los} and [Fe/H] for the whole spectroscopic dataset (including non-members) are given in Tables E.1 and E.2 available at the CDS. In addition, the *Gaia* DR3 parallax and proper motions are also provided, as well the proper motion membership determination. We also include information about the non-member stars that originally appeared to be spectroscopic members. With our new, larger, and more accurate dataset, we combined the 3D velocities of individual stars with their measured metallicities and took a look at the chemo-dynamical properties of the stellar population in the Sculptor dSph.

4.1. The VLT/FLAMES spectroscopic metallicities

We started by making a reanalysis of the mean metallicity in the Sculptor dSph. The CaT metallicities of individual RGB stars in Sculptor have previously been shown to be reliable as an [Fe/H] indicator, by comparing them to [Fe I/H] measurements for the same stars made with high-resolution spectra (e.g. Battaglia et al. 2008b; Starkenburg et al. 2010; Hill et al. 2019), and we have repeated this exercise in Appendix C (see Fig. C.1).

The metallicity distribution function (MDF) of the 1339 [Fe/H] measurements ($S/N > 13$) is shown in Fig. 15. A Gaussian is a reasonable match to the distribution. This could be marginally improved for a distribution with two distinct components (metal-poor and metal-rich). This is consistent with two distinct metallicity components (e.g. Tolstoy et al. 2004; Battaglia et al. 2008a). However, it is not clear that any metallicity distribution needs to be Gaussian. In addition, the distinction between two populations and a gradient is not easy to draw. In
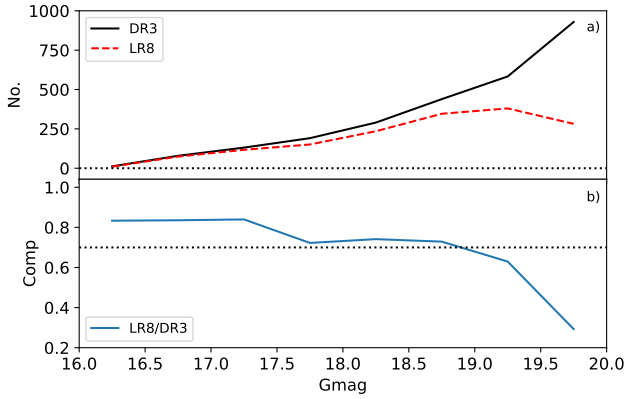
Fig. 13. Completeness of the VLT/FLAMES LR8 survey relative to *Gaia* DR3 for Sculptor members as a function of *Gaia* G magnitude: (a) the number of *Gaia* DR3 astrometric members (solid black line) and those with VLT/FLAMES LR8 spectroscopic confirmation (dashed red line), with a black dotted line at null; (b) the fraction of *Gaia* DR3 astrometric members that have a VLT/FLAMES LR8 spectrum with $S/N > 7$ and v_{los} consistent with membership in Sculptor. The black dotted line denotes 70%.
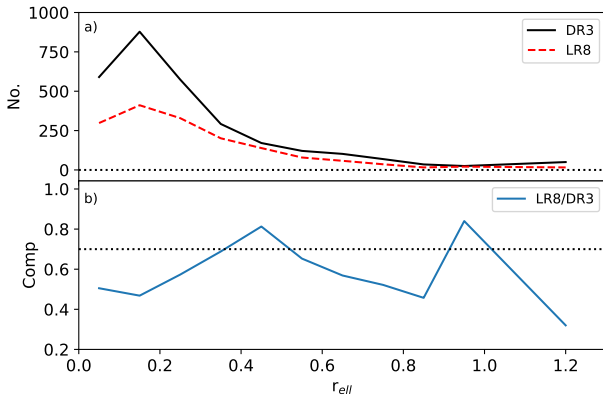

Fig. 14. Completeness of the VLT/FLAMES LR8 survey relative to *Gaia* DR3 for Sculptor members as a function of elliptical radius (r_{ell}): (a) the number of *Gaia* DR3 astrometric members (solid black line), and those with VLT/FLAMES LR8 spectroscopic confirmation (dashed red line), with a black dotted line at null; (b) fraction of *Gaia* DR3 astrometric members that have a VLT/FLAMES LR8 spectrum of sufficient S/N, >7, and a v_{los} consistent with membership. The dotted black line denotes 70%.

Table 1. Mean properties of the Sculptor dSph galaxy; the errors are the standard deviation.

Property	Mean	Previous
$\langle[\text{Fe/H}]\rangle$	-1.82 ± 0.45	-1.58 ± 0.41 [1]
$\langle v_{los} \rangle$ (km/s)	111.2 ± 0.25	110.6 ± 0.5 [2]
		111.4 ± 0.1 [3]
v_{los} ([Fe/H] > -1.7)	111.50 ± 0.36	
v_{los} ([Fe/H] < -1.7)	110.06 ± 0.37	
v_{los} ([Fe/H] < -2.2)	112.27 ± 0.67	
v_{los} ([Fe/H] < -2.5)	114.82 ± 1.37	
$\langle\mu_\alpha\rangle_{sp}$ (mas/yr)	0.097 ± 0.006	0.099 ± 0.002 [4]
$\langle\mu_\delta\rangle_{sp}$ (mas/yr)	-0.148 ± 0.004	-0.159 ± 0.002 [4]
$\langle\varpi\rangle_{sp}$ (mas)	0.004 ± 0.007	-0.013 ± 0.004 [5]

References. [1]Kirby et al. (2009). [2]Battaglia et al. (2008b). [3]Walker et al. (2009) [4]Battaglia et al. (2022), based on *Gaia* DR3. [5]Gaia Collaboration (2018b), based on *Gaia* DR2.
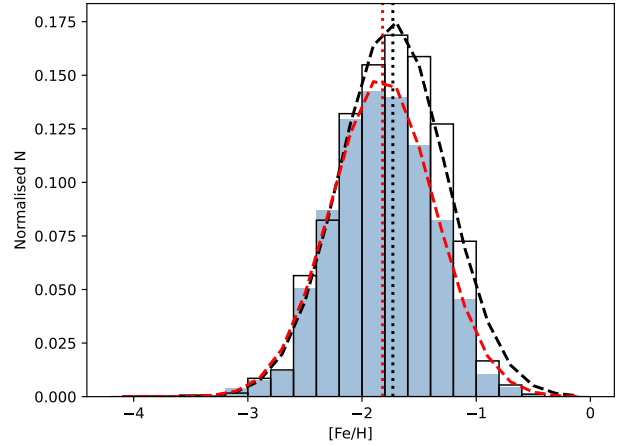
Fig. 15. MDF for the 1339 metallicity measurements of RGB members of the Sculptor dSph (blue). The vertical dotted red line is the mean, [Fe/H] $= -1.82$, as determined by a Gaussian fit to the distribution (dashed red line). The black-outlined histogram is corrected for the incompleteness at different elliptical radii, as given in Fig. 14. The mean metallicity shifts by about 0.1 dex (dotted black line) to [Fe/H] $= -1.73$, according to the Gaussian fit (dashed black line).

Fig. 15 we also show the MDF corrected for the incompleteness as a function of elliptical radius for the different radial bins as determined in Fig. 14 (as an open black histogram and a black dashed line Gaussian fit). This assumed that the *Gaia* DR3 RGB members are representative of the mass of stars in the galaxy. In Fig. 15 it can be seen that the effect is not likely to be large, if this assumption was reasonable. The shift in the mean of the population appears to be small, only ~0.1 dex. However, outliers cannot be corrected for as they are rare objects, so the prime reason to increase the completeness of the observations is to look for the true number of rare objects, such as extremely metal-poor stars or carbon-rich stars.

The fact that the central region of Sculptor was found to be significantly more metal-rich on average than the outer regions likely explains the higher average metallicity of Sculptor determined by Kirby et al. (2009), who focused on the inner regions of Sculptor (see Table 1). This could also be an offset in the calibration caused by different metallicity indicators used. It should be noted that in our CaT method metal-rich stars suffered more from low S/N than metal-poor stars, as the strong sky lines next to the middle line (EW2) can be problematic at low S/N and when the line was wide it tended to overlap more with the strong sky line residuals. In all methods lines get weaker as stars get more metal poor.

For the 1339 RGB stars in our sample of VLT/FLAMES LR8 spectra in the Sculptor dSph with accurate [Fe/H], we plot [Fe/H] as a function of elliptical radii, r_{ell}, in Fig. 16. Here we also plot the binned mean and the dispersion in each bin, which is consistent with a straight line fit. The clear metallicity gradient is consistent with what has previously been noted (e.g. Tolstoy et al. 2004; Kirby et al. 2009), although the scatter plot is much denser and more extended than previous results, showing that there is a lot of intrinsic scatter in [Fe/H] at any r_{ell}, and the very few points lying at particularly high or low metallicities typically appear to be robust members. For the bulk of the measurements the scatter was much larger than the intrinsic errors on the measurements. This is consistent with a galaxy experiencing extended star formation, as opposed to a limited burst, where less scatter in the metallicities might be expected. The mean metallicity in the central bin of Fig. 16 is [Fe/H] $= -1.65$ with a
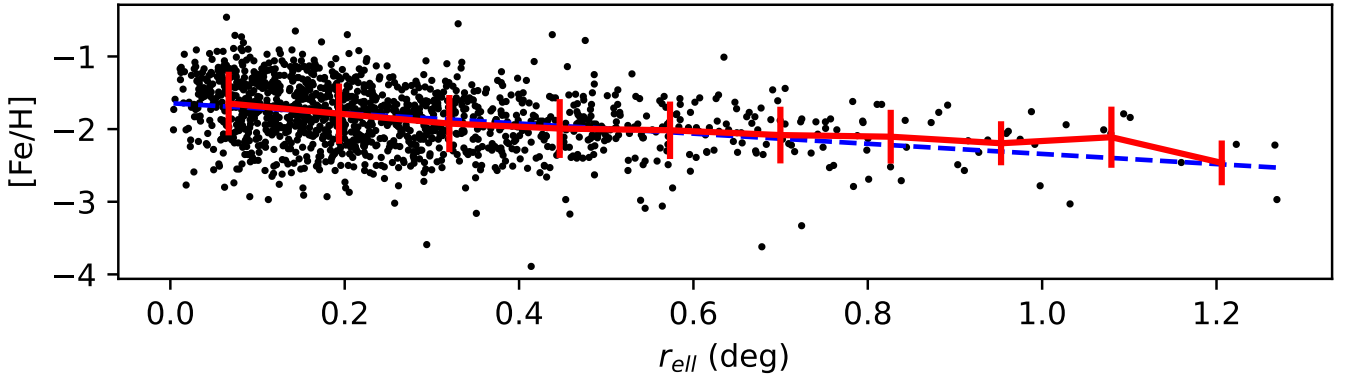
Fig. 16. [Fe/H] with elliptical radius, r_{ell}, which is the projected semi-major axis radius, for the 1339 measurements in our Sculptor sample. The dashed blue line shows the linear fit, which represents a gradient of -0.7 dex deg^{-1}. The red line shows the binned mean, and the error bars are the dispersion in each bin.
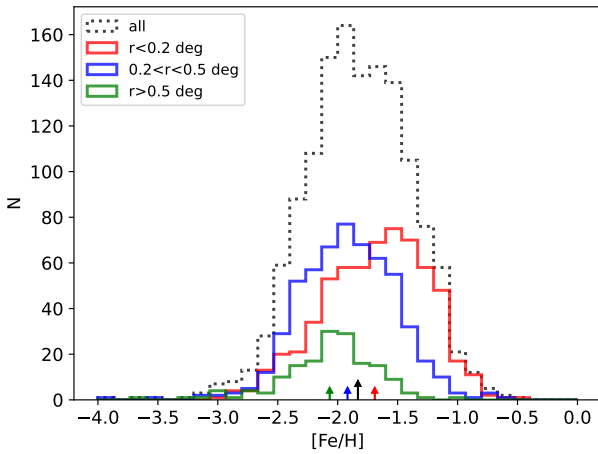

Fig. 17. VLT/FLAMES metallicities for 1339 RGB member stars at different ranges of elliptical radius (in degrees), r_{ell}, in the Sculptor dSph. Coloured arrows show the shift in mean metallicity for the different r_{ell} ranges.
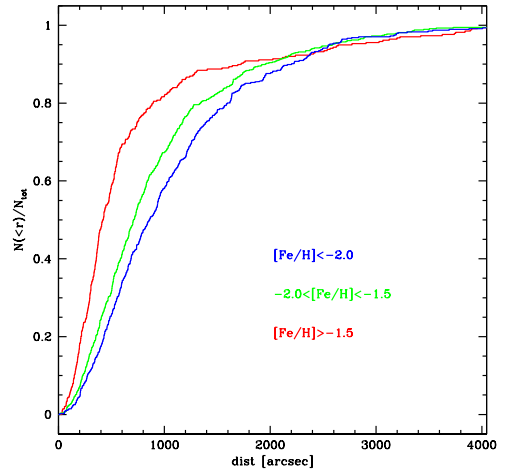

Fig. 18. Cumulative distributions for three sub-populations of member stars with different metallicities (colours), with increasing distance on the sky from the centre of the Sculptor.

dispersion of ±0.44 and in the outermost region the numbers of stars decrease dramatically, and the outermost bin in Fig. 16 contains four stars, and so the mean [Fe/H] = −2.47 with a dispersion of ±0.31 is not robust. Enlarging the last bin to outermost 8 or even 24 stars, leads to a mean [Fe/H] = −2.2 and a dispersion of ±0.36.

There is no clumpiness or any obvious signs of linear features that might suggest streams or groups of stars with similar metallicities and/or [Fe/H] values that differ from the mean. However, the dynamical timescale of a galaxy like Sculptor is very short (~50−100 Myr), and so evidence of past events will quickly disappear. Figure 16 also does not show an obvious presence of two populations, and it seems to be more consistent with a radial gradient and scatter around the typical metallicity at each radius. It still might be that different populations are hidden in the scatter. This is further explored in the next subsection, which includes the kinematics.

In general, the metal-poor population is consistently, if sparsely, distributed throughout the galaxy (Fig. 16), whereas the metal-rich component is clearly more centrally concentrated. This results in a mean metallicity gradient of −0.7 dex deg^{-1}. The intrinsic spread in metallicity seems to decrease towards the outer regions of Sculptor, but it is challenging to disentangle this

from the even more rapid fall in the number of measurements (representative of the falling stellar density). In Fig. 17 we show the metallicity gradient in the form of a histogram for different regions in elliptical radius. In Fig. 18 we show the cumulative radial distributions in three different metallicity ranges, with roughly equal numbers of stars, and it can be seen that the distributions differ, which is representative of the metallicity gradient seen in Figs. 16 and 17. These quantities are often derived by theoretical models and simulations of the stellar populations of dwarf galaxies (e.g. Gelli et al. 2020), and can be used as a reference for future comparisons.

4.2. The combined kinematic and metallicity properties

By adding v_{los} to the [Fe/H] measurements we can look at the chemo-dynamical properties of the Sculptor dSph. The normalised histogram of the 1604 v_{los} measurements ($S/N > 7$) in our new sample is shown in Fig. 19, along with a Gaussian fit and a vertical line at the mean systemic velocity (111.2 km s^{-1}; see Table 1). This looks to be a normal distribution with the possible exception of a higher number of stars at larger v_{los}. The tail is not a feature of low S/N measurements, as it remains even if only the high S/N (>13) measurements are included.
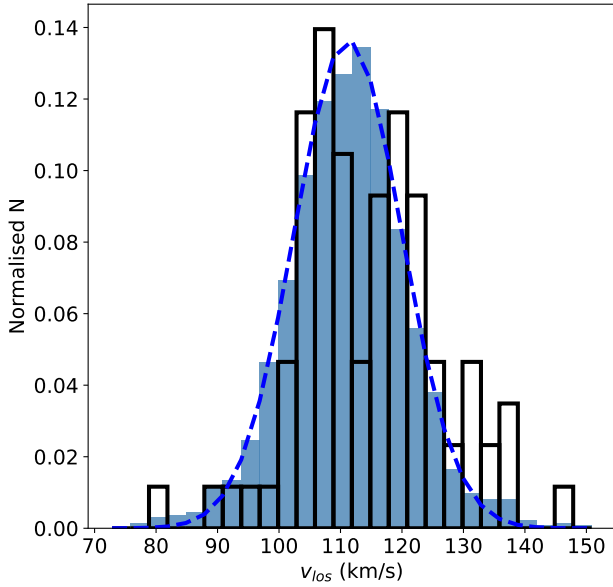
Fig. 19. Normalised histogram of VLT/FLAMES v_{los} measurements ($S/N > 13$) for the 1339 RGB members of the Sculptor dSph with reliable [Fe/H] determinations (blue). The shape of the distribution is fit with a Gaussian function (dashed blue line). In addition, the 86 stars with [Fe/H] < −2.5 are shown as a (black) open normalised histogram.

Also plotted in Fig. 19 is the normalised histogram distribution of the 86 stars with [Fe/H] ≤ −2.5. It clearly looks different the total distribution, falling into two peaks and extending very clearly to higher velocities. A Kolmogorov-Smirnov test was carried out, for the metallicity selections given in Table 1 and they all tend to be similar to each other, except at [Fe/H] < −2.2, where the difference starts to increase, and is significant only for [Fe/H] < −2.5. The stars with [Fe/H] < −2.5 have the most clear offset in mean velocity, partly because they are no longer a Gaussian distribution. This is barely significant given the errors and the small number of stars in this metallicity range, but it is a hint that the kinematics of the most metal population may be different and this should be followed up with larger samples.

To investigate the velocity and metallicity distribution in more detail, we plot the velocities of individual member stars against elliptical radius (r_{ell}), in Fig. 20, colour-coded by CaT metallicity ([Fe/H]). It can be clearly seen, as has already been established, that the metal-rich population is more centrally concentrated than the metal-poor population, and also has a lower velocity dispersion (Tolstoy et al. 2004; Battaglia et al. 2008a). The Sculptor stars withing the central region are now better studied, and the metal-rich population ([Fe/H] > −1.7) is shown to extend further out in the galaxy than previous smaller samples suggested. The highest metallicity stars show a marked central concentration, limited to $r_{ell} \lesssim 0.5$ deg. In addition, the velocity dispersion declines slightly moving from the centre of Sculptor (∼9 km s^{-1}) to the outermost regions with a dispersion of ∼4−6 km s^{-1}. In addition the central velocity also changes from 110.9 km s^{-1} in the inner regions to 116.5−117.5 km s^{-1} in the outer regions.

This new much larger and more accurate dataset appears to lack the rotation signature seen by Battaglia et al. (2008a), compatible with the results by Martínez-García et al. (2023). There is a slight gradient in the mean los velocity, ⟨v_{los}⟩, moving from the centre of Sculptor outwards. This is not an effect of the bulk motion of the galaxy projected onto the proper

motion and/or radial velocity at different positions in the galaxy (Feast et al. 1961; Feitzinger et al. 1977; Meatheringham et al. 1988; Kaplinghat & Strigari 2008), as assuming the proper motion given by Battaglia et al. (2022), and the distance from Martínez-Vázquez et al. (2015), the tangential motion of Sculptor is 74.4 km s^{-1}, and so the most significant v_{los} difference is 1.3 km s^{-1} [sin(ρ)], and this only leads to an apparent velocity gradient of 1.2 km s^{-1} deg^{-1}, which is not enough to explain what is seen in Fig. 20. The rotation of the Sun around the Milky Way compared to the position of Sculptor dSph on the sky results in a larger effect. In Fig. 21 we show the v_{los} corrected for the Galactic standard of rest, using the Gala python routine provided by Adrian M. Price-Whelan[6]. The mean velocities are plotted and the standard deviation is shown as a range of velocity. The mean v_{los} of stars in Sculptor increases by 6 km s^{-1} from the central region to the outskirts, giving a gradient of around +5 km s^{-1} deg^{-1}. Figure 21 suggests that this is a fairly symmetric effect from one side of the galaxy to the other, along the major axis. Changing the area around the major axis that is included in the plot makes no difference to the gradient. It can also been seen from the direction of the proper motion on the sky, given as a blue arrow in Fig. 12a, that the elongation of Sculptor is not along the direction of motion. However, the number of stars in the outer regions is relatively small, so the effect is not highly significant but it can be seen in both Figs. 20 and 21 that beyond $r_{ell} > 0.6$ deg the stars tend to have velocities higher than the systemic velocity. This could perhaps suggest that the outer regions of the galaxy are more loosely bound than the centre as might be expected for a small galaxy moving around in the tidal field of a much larger galaxy. There are no obvious clumpy velocity or velocity-metallicity structures, which could have suggested that the presence of dissolving globular clusters or other mergers events. It has been shown that interpreting the velocity structure in the outer regions of small dwarf galaxies orbiting in the potential of the Milky Way is not straightforward (van den Bosch et al. 2018). It is clear that to fully understand the complex dynamics of Sculptor careful dynamical modelling of this dataset will be needed. This is beyond the scope of this paper, but re-assessing in detail the internal chemo-dynamical properties of Sculptor will be the subject of future work.

4.3. The colour-magnitude diagram

In addition to the exquisite astrometry, the *Gaia* catalogue also includes uniquely accurate and well calibrated photometry in 3 photometric bands: G, G_{BP} and G_{RP} (Evans et al. 2018; Riello et al. 2021). The depth of the *Gaia* photometry for the Sculptor dSph (Fig. 12c, d) is quite a bit less than what has been possible from deep ground-based surveys (e.g. de Boer et al. 2011, 2012; Bettinelli et al. 2019), and certainly the *Hubble* Space Telescope (Dolphin 2002). However, the *Gaia* photometry is extremely well matched to our spectroscopic survey of the RGB, and it has the advantage of uniformly covering the whole galaxy on the sky.

One of the most stunning results comes from the excellence of the *Gaia* photometry. A clear metallicity gradient is seen across the RGB (Fig. 22), where the metal-rich and metal-poor populations lie along distinct isochrones, with the metallicity increasing with ($G_{BP} − G_{RP}$) colour. This is a much clearer distinction than has been seen before and is only possible because of the accurate and extensive *Gaia* DR3 photometry, combined

---

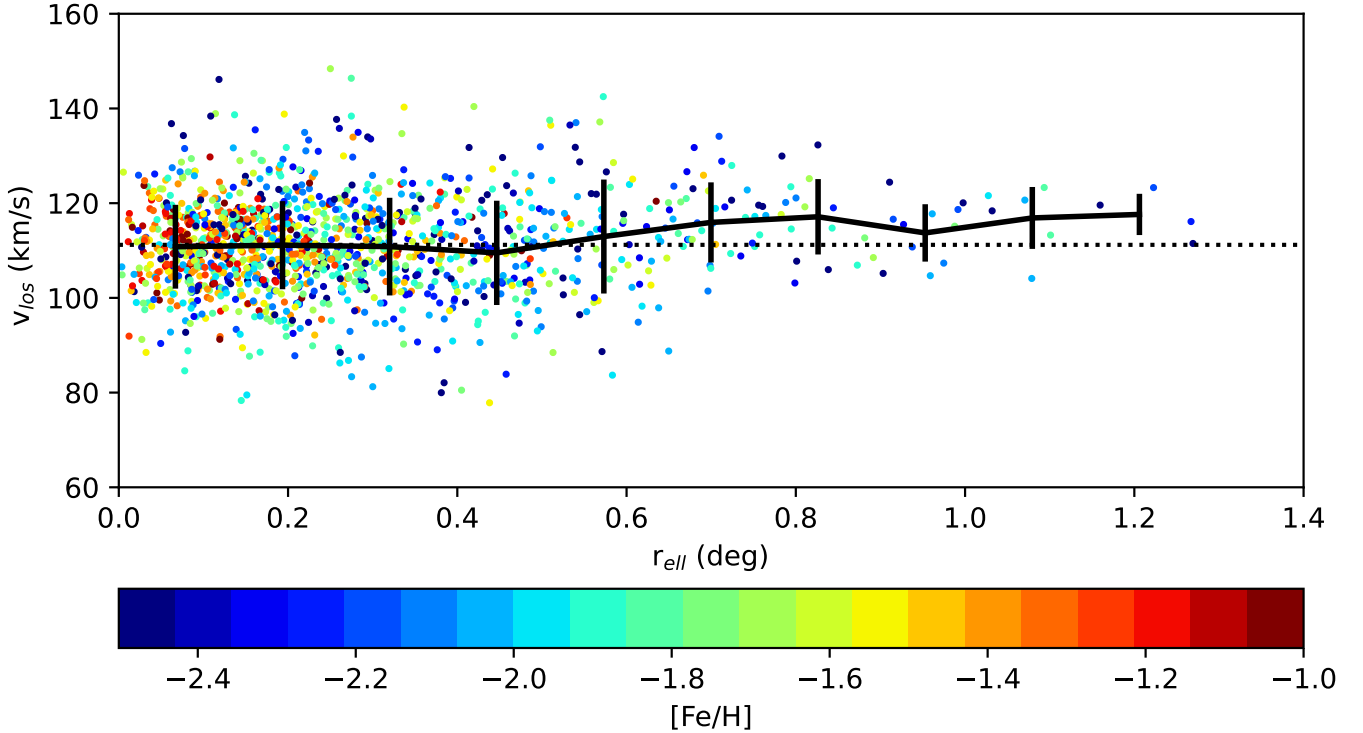[6] http://gala.adrian.pw/en/latest/api/gala.coordinates.vhel_to_vgsr.html

Fig. 20. VLT/FLAMES heliocentric los velocities, v_{los}, for the 1339 RGB stars in our sample with the most reliable [Fe/H] measurements as a function of elliptical radius, r_{ell}, in the Sculptor dSph. The dotted black line shows the mean $v_{los} = +111.2$ km s^{-1}, and the binned mean and the dispersion are plotted as a solid black line and error bars.

with the uniquely accurate membership determinations from *Gaia* DR3 astrometry and VLT/FLAMES los velocities. Plotted on top of the CMD in Fig. 22 are four isochrones taken from the α-rich ([α/Fe] = +0.4) a Bag of Stellar Tracks and Isochrones (BASTI) set (Hidalgo et al. 2018; Pietrinferni et al. 2021). The choice of isochrones is informed by the SFH of Sculptor (de Boer et al. 2012; Savino et al. 2018; Bettinelli et al. 2019), and high-resolution spectroscopic abundances (Hill et al. 2019). It is interesting to see the age-metallicity relation so clearly in the data and also how well they match the shape as well as the position of the isochrones. This comparison assumes a distance modulus, $m - M = 19.62$ and a reddening of $E(B - V) = 0.018$ (Battaglia et al. 2022). Arguably the most metal-rich isochrone ([Fe/H] = −1.4) should be solar-scaled ([α/Fe] = 0), as high-resolution spectroscopy in the central region shows that at this [Fe/H] the stars typically have [α/Fe] ≈ 0. However, this isochrone ([Fe/H] = −1.4, [α/Fe] = 0) did not fit the stellar distribution at all, even when increasing the age to 13 Gyr. A detailed analysis of the CMD is left to future work.

On the red side of the RGB are typically Carbon-rich stars (Fig. 23), many of which have been first identified by Azzopardi et al. (1985). They are likely to be dominated by stars that have been enriched by interactions with a binary companion. Intrinsically carbon-enhanced metal-poor (CEMP) stars are more likely to be found more on the blue (metal-poor) side of the RGB. For example, the CEMP-no star found by Skúladóttir et al. (2015b), ET0097, is on the blue edge of the RGB (see Fig. 23). On the blue side of the RGB is where the most metal-poor stars are to be found, as is shown in Fig. 22. The scatter far from the RGB is most likely due to stars following unusual evolutionary tracks (e.g. ET0048 from Hill et al. 2019); they could be "rejuvenated" blue-straggler type objects, of which there are quite a few on the main sequence (e.g. Mapelli et al. 2009), where they stand

out more clearly. There are certainly ancient asymptotic giant branch (AGB) stars in the Sculptor *Gaia* DR3 CMD. Looking at dedicated AGB isochrones (e.g. Marigo et al. 2013) to fit the outliers beside and above the RGB requires extremely young ages (∼2–4 Gyr), which are clearly inconsistent with the SFH determined from the much more reliable and much more populated main sequence turnoff region (e.g. de Boer et al. 2012). Thus if these stars are AGB stars, and thus members of Sculptor, they are likely to be stars that have been rejuvenated by binary interactions. In Fig. 23, for consistency we use the BASTI isochrones, which show the early AGB phase. It is clear that they overlap with the RGB, especially on the blue side: younger, more metal-rich AGB stars are likely to overlap with older, more metal-poor RGB stars. Dedicated AGB models (Marigo et al. 2013) go to higher luminosities, up to and above the tip of the RGB and might explain more of the scatter here in Fig. 23. Picking out the AGB stars is important for the purposes of understanding the spectroscopic results in terms of chemical evolution and SFH. The AGB phase can potentially explain some of the metal-poor stars bluer than the bulk of the RGB. The distinction between an AGB and an RGB star is difficult to make observationally, even on the basis of HR spectroscopy. However, they are expected to have excess carbon in their spectra due to the various dredge up and mixing processes that occur during the AGB stellar evolution phase. A detailed analysis of these evolved stars in Sculptor is left to a future work.

4.4. The most metal-poor stars

For the past two decades, astronomers have searched the Sculptor dSph looking for extremely metal-poor stars (e.g. Tolstoy et al. 2003; Tafelmeyer et al. 2010; Frebel et al. 2010; Starkenburg et al. 2013; Jablonka et al. 2015; Simon et al. 2015;
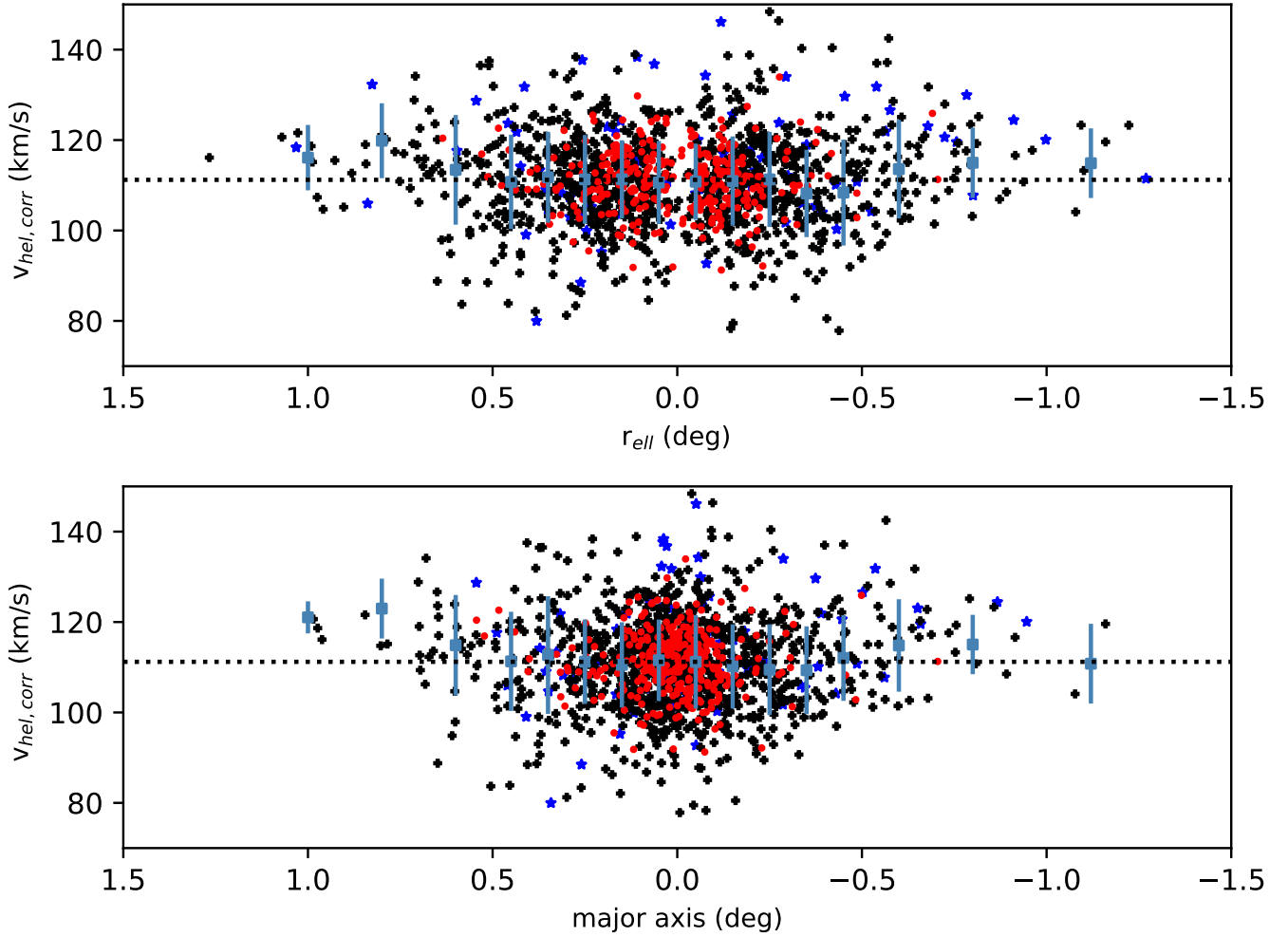
Fig. 21. VLT/FLAMES LR v_{los} corrected for the shift created by the motion of the Sun around the Galactic centre at the position of Sculptor, colour-coded by [Fe/H], as a function of elliptical radius, r_{ell} (top) and the position along the major axis (bottom). The colour-code is blue stars: [Fe/H] < −2.5; black crosses −2.5 ≤ [Fe/H] < −1.5; and red circles [Fe/H] ≥ −1.5. Binned mean velocities are shown as steel blue points, with their standard deviation as bars.

Skúladóttir et al. 2015b, 2021; Chiti et al. 2018; Hill et al. 2019). These searches have been less fruitful than originally expected, and although there are a couple of stars around [Fe/H] ∼ −4, the extremely metal-poor tail ([Fe/H] < −3) is not well populated. Another interesting aspect is the lack of CEMP stars without s-process enhancement (CEMP-no). These are progressively more common in the Galactic halo, and in ultra-faint dwarf galaxies at [Fe/H] < −2. There are one or two unambiguous examples of these stars in the Sculptor dSph, a conspicuous absence compared to the Milky Way and ultra-faint dwarfs (e.g. Skúladóttir et al. 2015b; Salvadori et al. 2015; Kirby et al. 2015). Of the known sample of C-rich stars from Azzopardi et al. (1985), two appear to be metal poor, and could possibly be CEMP-no stars. The rest are more likely to be highly evolved carbon stars or CEMP-s stars, but limited high-resolution spectroscopy has been carried out on this sample due to the complexities of dealing with strong C features in the spectra. In some of the more extreme cases it is even challenging to accurately determine [Fe/H].

In Fig. 23 we show in the CMD, both extremely metal-poor ([Fe/H] < −3) RGB stars in our Sculptor VLT/FLAMES LR8 sample, and also where C-rich stars have been found. Most of the bright VLT/FLAMES targets with [Fe/H] < −2.5 have already been observed with follow-up intermediate- to high-resolution spectra, although in a few cases the analysis is still pending. In Fig. 23 we also identify some of the stars that have been followed up with high resolution spectroscopic abundance analysis. Of the stars with metallicity [Fe/H] < −3, Scl03111 ([Fe/H] = −3.61) is from Jablonka et al. (2015), and S1020549 is from Frebel et al. (2010), originally given as [Fe/H] = −3.81, but reanalysed by Simon et al. (2015) to have [Fe/H] = −3.68. Scl07-50 is the most metal-poor star in the Tafelmeyer et al. (2010) sample, at [Fe/H] = −3.96, but reanalysed by Simon et al. to have [Fe/H] = −4.05. There is also Scl07-49, analysed by Tafelmeyer et al. to have [Fe/H] = −3.48, and re-analysed by Simon et al. to be [Fe/H] = −3.28. The star AS0039 has been analysed by Skúladóttir et al. (2021) to have [Fe/H] = −4.11, and is thus currently the most metal-poor star known in Sculptor dSph. The most metal-poor isochrones match the positions of these stars quite well, and none of them appear to be an obvious AGB candidate, given how metal-poor they are. Only some of the stars further to the blue from the main RGB or above the tip of the RGB are likely to be AGB stars. A more detailed analysis of the stars that do not match the isochrone positions is needed to see if there are AGB stars buried in the RGB population. This distinction is not easy to make on the basis of spectroscopy.
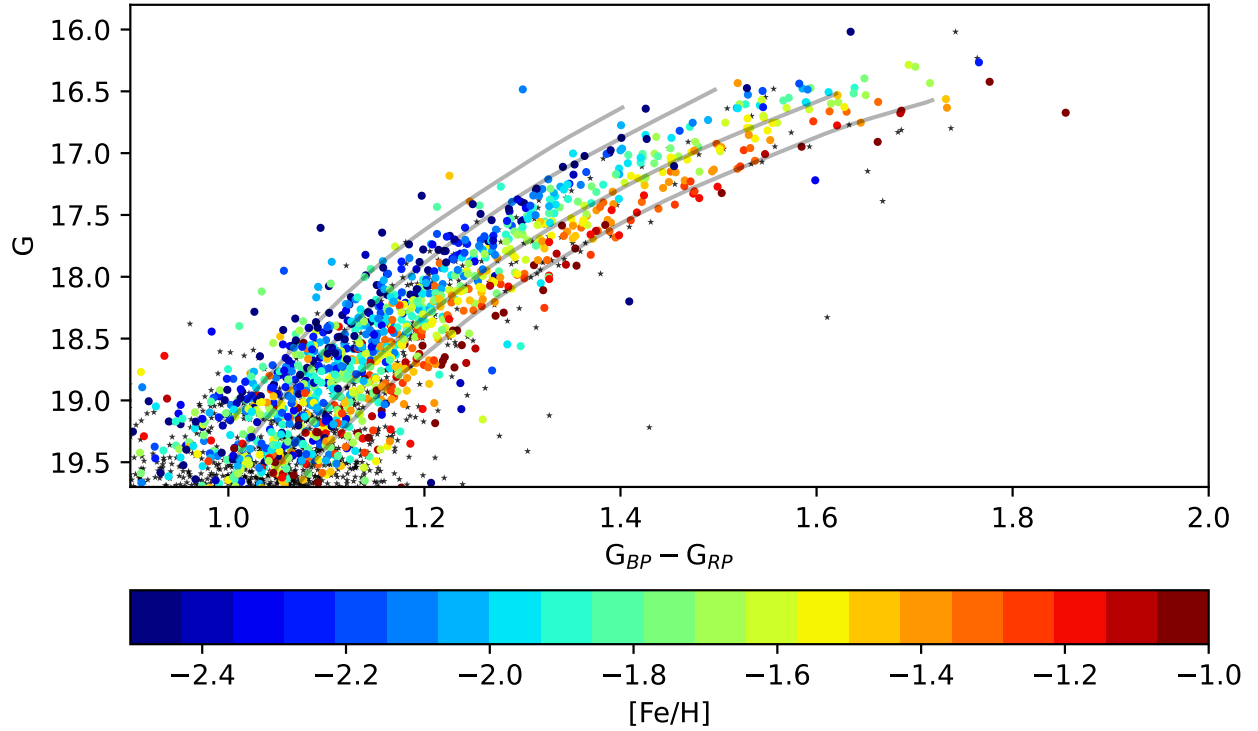
Fig. 22. *Gaia* DR3 CMD for the 1339 ($S/N > 13$) members of the Sculptor dSph, colour-coded by [Fe/H]. Small black stars are *Gaia* DR3 members without VLT/FLAMES spectroscopy or insufficiently accurate [Fe/H] measurements. Grey lines are BASTI RGB isochrones, with [α/Fe]= +0.4, for (from left to right): [Fe/H] = −3.2, −2.2, −1.7, −1.4; and age = 13, 13, 12, 10 Gyr.

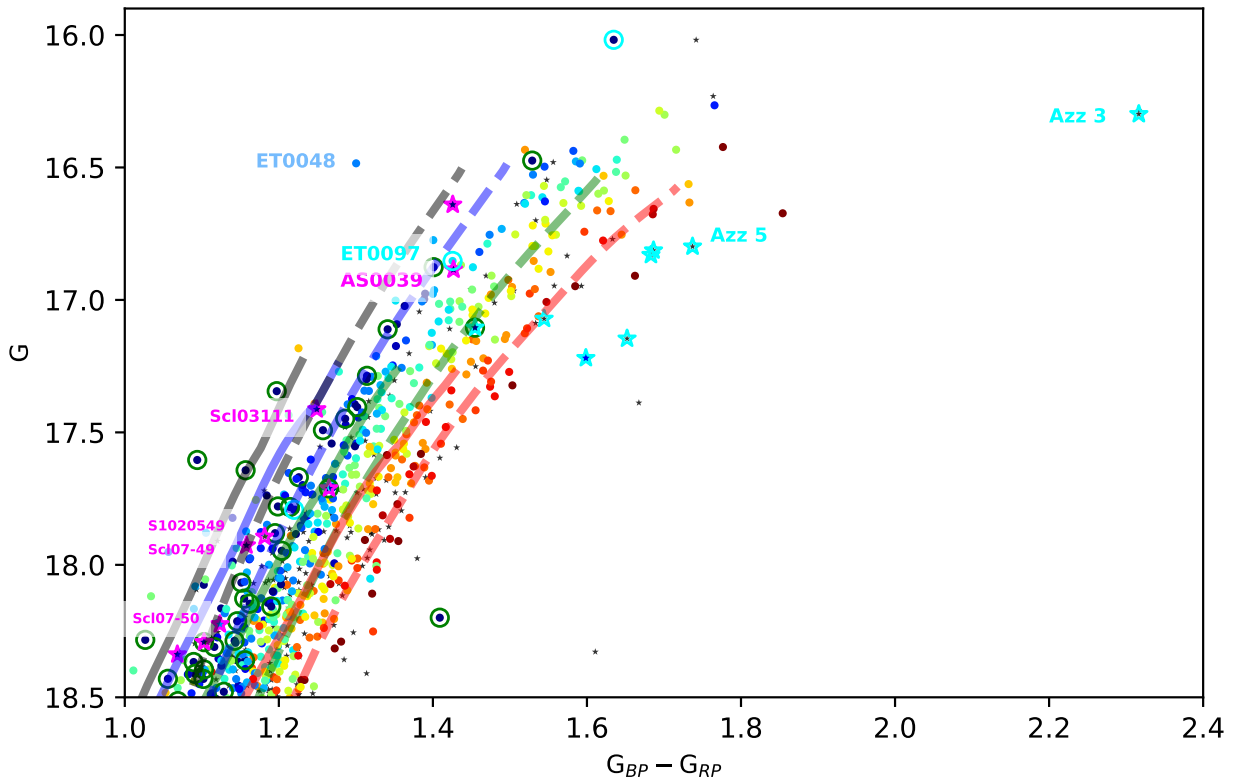**Fig. 23.** Upper *Gaia* DR3 CMD for all members of the Sculptor dSph, colour-coded by [Fe/H] as in Fig. 22. The eight cyan stars symbols come from the carbon star catalogue of Azzopardi et al. (1985), and the three open cyan circles are C-rich stars from later studies. Magenta star symbols are stars with [Fe/H] < −3 in our sample, while green circles are those with −3 < [Fe/H] < −2.5. BASTI isochrones from Fig. 22 are in dashed coloured lines, with the early AGB evolutionary phase shown as solid lines.

5. Conclusions

With a combination of new and old re-processed archival VLT/FLAMES LR8 data, we have obtained a uniform sample of [Fe/H], v_{los}, and *Gaia* DR3 astrometric parameters for 1604 individual member RGB stars. This is the largest sample of individual measurements made to date for a classical dSph galaxy, and they extend from the inner regions to the outermost. This has allowed us to look again at the chemo-dynamical properties of the Sculptor dSph. The main difference with previous results is that, because of the much larger, more uniformly distributed, and more precise 'cleaner' sample, we see more members of different sub-populations; thus the scatter is much better quantified and the differences become subtler. This will allow more sophisticated and detailed modelling of this galaxy.

We confirm that the Sculptor dSph has complex v_{los} and [Fe/H] distributions. We present a new and more complete MDF for Sculptor, including a correction for the incompleteness of the spectroscopic data. We no longer find the rotation signature from earlier work with part of this sample. The kinematic differences between metal-rich and metal-poor populations appear more intricate than originally thought, with the strongest differences in the global properties being found in this analysis for the 86 most metal-poor stars. The wealth of information coming from the combination of spectroscopic metallicities and the exquisite photometry of the Sculptor dSph RGB reveals the complex buildup of metals and the subtler and more difficult-to-interpret motions of the stars within the galaxy.

References

Aaronson, M., & Olszewski, E. W. 1987, AJ, 94, 657
Agnello, A., & Evans, N. W. 2012, ApJ, 754, L39
Armandroff, T. E., & Da Costa, G. S. 1986, AJ, 92, 777
Azzopardi, M., Lequeux, J., & Westerlund, B. E. 1985, A&A, 144, 388
Baade, W., & Hubble, E. 1939, PASP, 51, 40
Bailer-Jones, C. A. L., Rybizki, J., Fouesneau, M., Demleitner, M., & Andrae, R. 2021, AJ, 161, 147
Battaglia, G., & Starkenburg, E. 2012, A&A, 539, A123
Battaglia, G., Helmi, A., Tolstoy, E., et al. 2008a, ApJ, 681, L13
Battaglia, G., Irwin, M., Tolstoy, E., et al. 2008b, MNRAS, 383, 183
Battaglia, G., Helmi, A., & Breddels, M. 2013, New A Rv., 57, 52
Battaglia, G., Taibi, S., Thomas, G. F., & Fritz, T. K. 2022, A&A, 657, A54
Bettinelli, M., Hidalgo, S. L., Cassisi, S., et al. 2019, MNRAS, 487, 5862
Breddels, M. A., & Helmi, A. 2013, A&A, 558, A35
Breddels, M. A., Helmi, A., van den Bosch, R. C. E., van de Ven, G., & Battaglia, G. 2013, MNRAS, 433, 3173
Cantat-Gaudin, T., Fouesneau, M., Rix, H.-W., et al. 2023, A&A, 669, A55
Carrera, R., Pancino, E., Gallart, C., & del Pino, A. 2013, MNRAS, 434, 1681
Cayrel, R., Depagne, E., Spite, M., et al. 2004, A&A, 416, 1117
Chiti, A., Simon, J. D., Frebel, A., et al. 2018, ApJ, 856, 142
Clementini, G., Ripepi, V., Bragaglia, A., et al. 2005, MNRAS, 363, 734
Da Costa, G. S. 1984, ApJ, 285, 483
de Boer, T. J. L., Tolstoy, E., Saha, A., et al. 2011, A&A, 528, A119
de Boer, T. J. L., Tolstoy, E., Hill, V., et al. 2012, A&A, 539, A103
Dekel, A., & Silk, J. 1986, ApJ, 303, 39
de los Reyes, M. A. C., Kirby, E. N., Ji, A. P., & Nuñez, E. H. 2022, ApJ, 925, 66
Demers, S., Krautter, A., & Kunkel, W. E. 1980, AJ, 85, 1587
Dolphin, A. E. 2002, MNRAS, 332, 91
Evans, D. W., Riello, M., De Angeli, F., et al. 2018, A&A, 616, A4
Fabricius, C., Luri, X., Arenou, F., et al. 2021, A&A, 649, A5
Feast, M. W., Thackeray, A. D., & Wesselink, A. J. 1961, MNRAS, 122, 433
Feitzinger, J. V., Isserstedt, J., & Schmidt-Kaler, T. 1977, A&A, 57, 265
Fenner, Y., Gibson, B. K., Gallino, R., & Lugaro, M. 2006, ApJ, 646, 184
Ferrara, A., & Tolstoy, E. 2000, MNRAS, 313, 291
Frebel, A., Kirby, E. N., & Simon, J. D. 2010, Nature, 464, 72
Freudling, W., Romaniello, M., Bramich, D. M., et al. 2013, A&A, 559, A96
Gaia Collaboration (Prusti, T., et al.) 2016, A&A, 595, A1
Gaia Collaboration (Brown, A. G. A., et al.) 2018a, A&A, 616, A1
Gaia Collaboration (Helmi, A., et al.) 2018b, A&A, 616, A12
Gaia Collaboration (Brown, A. G. A., et al.) 2021, A&A, 649, A1
Gaia Collaboration (Klioner, S. A., et al.) 2022, A&A, 667, A148
Gaia Collaboration (Vallenari, A., et al.) 2023, A&A, 674, A1
Geisler, D., Smith, V. V., Wallerstein, G., Gonzalez, G., & Charbonnel, C. 2005, AJ, 129, 1428
Gelli, V., Salvadori, S., Pallottini, A., & Ferrara, A. 2020, MNRAS, 498, 4134
Gilmore, G., & Wyse, R. F. G. 1991, ApJ, 367, L55
Harbeck, D., Grebel, E. K., Holtzman, J., et al. 2001, AJ, 122, 3092
Hidalgo, S. L., Pietrinferni, A., Cassisi, S., et al. 2018, ApJ, 856, 125
Hill, V., Skúladóttir, Á., Tolstoy, E., et al. 2019, A&A, 626, A15
Hurley-Keller, D., Mateo, M., & Grebel, E. K. 1999, ApJ, 523, L25
Iorio, G., Nipoti, C., Battaglia, G., & Sollima, A. 2019, MNRAS, 487, 5692
Irwin, M., & Hatzidimitriou, D. 1995, MNRAS, 277, 1354
Jablonka, P., North, P., Mashonkina, L., et al. 2015, A&A, 583, A67
Kaluzny, J., Kubiak, M., Szymanski, M., et al. 1995, A&AS, 112, 407
Kaplinghat, M., & Strigari, L. E. 2008, ApJ, 682, L93
Kirby, E. N., Guhathakurta, P., Bolte, M., Sneden, C., & Geha, M. C. 2009, ApJ, 705, 328
Kirby, E. N., Guhathakurta, P., Simon, J. D., et al. 2010, ApJS, 191, 352
Kirby, E. N., Guo, M., Zhang, A. J., et al. 2015, ApJ, 801, 125
Kirby, E. N., Xie, J. L., Guo, R., et al. 2019, ApJ, 881, 45
Lanfranchi, G. A., & Matteucci, F. 2004, MNRAS, 351, 1338
Lardo, C., Battaglia, G., Pancino, E., et al. 2016, A&A, 585, A70
Lindegren, L., Bastian, U., Biermann, M., et al. 2021, A&A, 649, A4
Łokas, E. L. 2009, MNRAS, 394, L102
Mapelli, M., Ripamonti, E., Battaglia, G., et al. 2009, MNRAS, 396, 1771
Marcolini, A., D'Ercole, A., Battaglia, G., & Gibson, B. K. 2008, MNRAS, 386, 2173
Marigo, P., Bressan, A., Nanni, A., Girardi, L., & Pumo, M. L. 2013, MNRAS, 434, 488
Martínez-García, A. M., del Pino, A., & Aparicio, A. 2023, MNRAS, 518, 3083
Martínez-Vázquez, C. E., Monelli, M., Bono, G., et al. 2015, MNRAS, 454, 1509
Massari, D., Breddels, M. A., Helmi, A., et al. 2018, Nat. Astron., 2, 156
McConnachie, A. W., & Venn, K. A. 2020, AJ, 160, 124
Meatheringham, S. J., Dopita, M. A., Ford, H. C., & Webster, B. L. 1988, ApJ, 327, 651
Monkiewicz, J., Mould, J. R., Gallagher, John S., I., , et al. 1999, PASP, 111, 1392
Norris, J., & Bessell, M. S. 1978, ApJ, 225, L49
Pietrinferni, A., Hidalgo, S., Cassisi, S., et al. 2021, ApJ, 908, 102
Queloz, D., Dubath, P., & Pasquini, L. 1995, A&A, 300, 31
Reichert, M., Hansen, C. J., Hanke, M., et al. 2020, A&A, 641, A127
Revaz, Y., & Jablonka, P. 2018, A&A, 616, A96
Revaz, Y., Jablonka, P., Sawala, T., et al. 2009, A&A, 501, 189
Riello, M., De Angeli, F., Evans, D. W., et al. 2021, A&A, 649, A3
Romano, D., & Starkenburg, E. 2013, MNRAS, 434, 471
Salgado, C., Da Costa, G. S., Norris, J. E., & Yong, D. 2019, MNRAS, 484, 3093
Salvadori, S., & Ferrara, A. 2009, MNRAS, 395, L6
Salvadori, S., Ferrara, A., & Schneider, R. 2008, MNRAS, 386, 348
Salvadori, S., Skúladóttir, Á., & Tolstoy, E. 2015, MNRAS, 454, 1320
Savino, A., de Boer, T. J. L., Salaris, M., & Tolstoy, E. 2018, MNRAS, 480, 1587
Shetrone, M. D., Briley, M., & Brewer, J. P. 1998, A&A, 335, 919
Shetrone, M., Venn, K. A., Tolstoy, E., et al. 2003, AJ, 125, 684
Simon, J. D. 2018, ApJ, 863, 89
Simon, J. D., Jacobson, H. R., Frebel, A., et al. 2015, ApJ, 802, 93
Skúladóttir, Á., Andrievsky, S. M., Tolstoy, E., et al. 2015a, A&A, 580, A129
Skúladóttir, Á., Tolstoy, E., Salvadori, S., et al. 2015b, A&A, 574, A129

Skúladóttir, Á., Tolstoy, E., Salvadori, S., Hill, V., & Pettini, M. 2017, A&A, 606, A71

Skúladóttir, Á., Salvadori, S., Pettini, M., Tolstoy, E., & Hill, V. 2018, A&A, 615, A137

Skúladóttir, Á., Hansen, C. J., Salvadori, S., & Choplin, A. 2019, A&A, 631, A171

Skúladóttir, Á., Hansen, C. J., Choplin, A., et al. 2020, A&A, 634, A84

Skúladóttir, Á., Salvadori, S., Amarsi, A. M., et al. 2021, ApJ, 915, L30

Skúladóttir, Á., Puls, A. A., Amarsi, A. M., et al. 2023, The Messenger, 190, 19

Starkenburg, E., Hill, V., Tolstoy, E., et al. 2010, A&A, 513, A34

Starkenburg, E., Hill, V., Tolstoy, E., et al. 2013, A&A, 549, A88

Starkenburg, E., Martin, N., Youakim, K., et al. 2017, MNRAS, 471, 2587

Strigari, L. E., Frenk, C. S., & White, S. D. M. 2017, ApJ, 838, 123

Tafelmeyer, M., Jablonka, P., Hill, V., et al. 2010, A&A, 524, A58

Tang, B., Zhang, J., Yan, Z., et al. 2023, A&A, 669, A125

Tolstoy, E., Irwin, M. J., Cole, A. A., et al. 2001, MNRAS, 327, 918

Tolstoy, E., Venn, K. A., Shetrone, M., et al. 2003, AJ, 125, 707

Tolstoy, E., Irwin, M. J., Helmi, A., et al. 2004, ApJ, 617, L119

van den Bosch, F. C., Ogiya, G., Hahn, O., & Burkert, A. 2018, MNRAS, 474, 3043

Walker, M. G., & Peñarrubia, J. 2011, ApJ, 742, 20

Walker, M. G., Mateo, M., & Olszewski, E. W. 2009, AJ, 137, 3100

Weisz, D. R., Dolphin, A. E., Skillman, E. D., et al. 2014, ApJ, 789, 147

Wenger, M., Ochsenbein, F., Egret, D., et al. 2000, A&AS, 143, 9

Zhu, L., van de Ven, G., Watkins, L. L., & Posti, L. 2016, MNRAS, 463, 1117

Appendix A: The Observations: Individual VLT/FLAMES pointings

Table A.1. Sculptor LR8 observations with VLT/FLAMES/GIRAFFE.

No.	Date	Name	Prog ID	Centre of field		airm	DIMM	exp	spec	vmem	vshift
1	2003.09.29	Scl02a	171.B-0588	00 58 22.4	-33 42 36.0	1.52	0.95	1800	104	63	1.125
-	2003.09.29	Scl02b	171.B-0588	00 58 22.4	-33 42 36.0	1.32	0.99	1800	99	60	0.821
2	2003.09.29	Scl11a	171.B-0588	00 56 08.9	-33 42 29.0	2.12	1.06	1200	41	14	0.544
-	2003.09.29	Scl11b	171.B-0588	00 56 08.9	-33 42 29.0	1.80	1.02	1800	55	22	0.658
-	2003.09.30	Scl11c	171.B-0588	00 56 09.0	-33 42 29.0	1.13	0.60	1800	54	18	1.404
3	2003.09.30	Scl04a	171.B-0588	00 59 55.4	-33 15 53.8	1.92	0.79	1800	68	16	0.764
-	2003.09.30	Scl04b	171.B-0588	00 59 55.4	-33 15 53.8	1.58	0.61	1800	73	20	0.423
4	2003.09.30	Scl07	171.B-0588	01 00 10.9	-34 06 04.0	1.37	0.74	3600	76	38	0.541
5	2003.10.01	Scl03a	171.B-0588	01 01 44.1	-33 43 01.5	1.32	0.60	1800	113	83	0.92
-	2003.10.01	Scl03b	171.B-0588	01 01 44.1	-33 43 01.5	1.21	0.55	1800	113	78	0.916
6	2003.10.01	Scl05a	171.B-0588	00 58 08.8	-33 10 42.3	1.83	–	1800	11	0	0.771
-	2003.10.01	Scl05b	171.B-0588	00 58 08.8	-33 10 42.3	1.49	0.58	1800	45	14	0.555
7	2003.10.02	Scl025a	171.B-0588	00 59 46.4	-32 40 00.7	2.20	0.51	1200	22	4	1.012
-	2003.10.02	Scl025b	171.B-0588	00 59 46.4	-32 40 00.7	1.84	0.69	1554	25	4	1.061
8	2004.08.14	Scl14a	171.B-0588	01 03 29.6	-33 40 47.2	1.09	0.44	3600	52	19	0.793
-	2004.10.12	Scl14b	171.B-0588	01 03 29.6	-33 40 47.2	1.05	0.60	3600	52	24	0.791
9	2004.10.11	Scl20	171.B-0588	01 06 14.5	-33 41 23.4	1.08	0.90	3600	33	4	1.146
10	2004.09.10	SclCen	072.D-0245	01 00 03.8	-33 41 29.7	1.08	0.86	3600	114	99	0.439
11	2005.11.07	Scl103a	076.B-0391	00 57 24.8	-33 34 37.7	1.18	0.68	3600	71	45	0.941
-	2005.11.07	Scl103b	076.B-0391	00 57 24.8	-33 34 37.7	1.01	0.92	3600	71	51	0.928
12	2005.11.07	Scl109	076.B-0391	01 01 11.3	-33 56 50.8	1.04	0.60	3600	98	80	1.001
13	2005.11.07	Scl106	076.B-0391	01 01 23.7	-33 23 39.7	1.15	0.68	3600	85	50	0.269
14	2005.11.07	Scl101	076.B-0391	01 02 52.3	-33 52 06.0	1.06	1.13	3600	52	19	1.153
15	2005.11.08	Scl108a	076.B-0391	00 58 59.9	-33 27 04.9	1.13	1.21	2700	95	70	0.736
-	2005.11.08	Scl108b	076.B-0391	00 58 59.9	-33 27 04.9	1.25	1.01	2700	95	48	0.916
16	2007.06.21	Scl207	079.B-0435	01 03 52.5	-34 12 59.8	1.22	1.05	3600	37	14	3.065
17	2007.06.21	Scl203	079.B-0435	01 04 35.0	-33 24 40.2	1.53	0.78	3600	31	7	0.207
18	2007.06.21	Scl200a	079.B-0435	01 05 10.4	-33 49 04.9	1.12	0.88	3600	36	10	-3.338
-	2007.06.21	Scl200b	079.B-0435	01 05 10.4	-33 49 04.9	1.03	1.08	1800	36	8	-3.448
19	2007.08.14	Scl202a	079.B-0435	00 54 23.1	-33 31 44.9	1.01	0.54	1800	28	3	-0.128
-	2007.09.14	Scl202b	079.B-0435	00 54 23.1	-33 31 44.9	1.22	0.94	3600	30	7	0.227
20	2007.09.12	Scl220	079.B-0435	01 03 13.2	-33 13 01.5	1.11	1.22	3600	46	12	0.834
21	2007.09.13	Scl204a	079.B-0435	01 00 38.2	-32 59 40.1	1.11	–	3600	30	3	-3.324
-	2007.09.14	Scl204b	079.B-0435	01 00 38.2	-32 59 40.1	1.02	0.67	1800	32	4	0.416
22	2007.09.14	Scl211	079.B-0435	00 56 12.6	-34 02 10.6	1.07	1.38	3600	42	6	-8.377
23	2007.09.14	Scl209	079.B-0435	00 57 48.8	-34 18 41.2	1.13	1.23	3600	41	12	-0.280
24	2007.09.14	Scl206a	079.B-0435	00 59 34.4	-34 21 34.6	1.21	1.61	1800	48	7	-0.388
-	2007.09.15	Scl206b	079.B-0435	00 59 34.4	-34 21 34.6	1.03	1.11	3600	48	11	-7.877
25	2007.09.15	Scl205	079.B-0435	01 01 57.6	-34 17 39.2	1.02	1.25	3600	54	9	-0.183
26	2007.09.16	Scl208	079.B-0435	00 58 50.9	-33 58 15.9	1.08	1.05	3600	97	63	-8.264
27	2007.12.04	Scl201	079.B-0435	00 55 59.5	-33 13 31.1	1.28	1.88	3600	37	5	-1.870
28	2014.07.20	SclB1	593.D-0309	00 59 27.0	-33 37 47.4	1.24	0.76	2700	96	96	0.071
-	2014.07.21	SclB2	593.D-0309	00 59 27.0	-33 37 47.4	1.14	0.81	2700	96	96	-0.204
-	2014.07.30	SclB3	593.D-0309	00 59 27.0	-33 37 47.4	1.38	0.68	2700	96	96	2.903
-	2014.08.16	SclB4	593.D-0309	00 59 27.0	-33 37 47.4	1.25	0.71	2700	96	96	0.232
-	2014.08.19	SclB5	593.D-0309	00 59 27.0	-33 37 47.4	1.16	1.35	2700	96	96	0.811
-	2014.10.24	SclB6	593.D-0309	00 59 27.0	-33 37 47.4	1.15	1.03	2700	96	96	0.323
-	2015.07.18	SclB7	593.D-0309	00 59 27.0	-33 37 47.4	1.06	1.31	2700	96	96	1.575
-	2015.10.04	SclB8	593.D-0309	00 59 27.0	-33 37 47.4	1.01	0.94	2700	96	96	2.166
29	2016.10.21	SclB9	098.D-0160	00 59 27.0	-33 37 47.4	1.50	0.96	2700	98	97	1.274

Table A.1. continued.

No.	Date	Name	Prog ID	Centre of field		airm	DIMM	exp	spec	vmem	vshift
30	2017.10.13	SclPM	0100.B-0337	01 00 05.5	-33 50 32.5	1.02	0.56	3600	115	112	2.134
31	2017.10.13	SclCen3	0100.B-0337	01 00 13.4	-33 40 45.3	1.23	0.45	3600	114	112	1.471
-	2017.10.13	SclCen2	0100.B-0337	01 00 13.4	-33 40 45.3	1.08	0.46	3600	115	113	1.646
32	2017.10.25	SclOut1	0100.B-0337	01 01 19.5	-33 42 58.5	1.04	0.78	3600	66	62	2.100
33	2018.09.09	SclC01	0101.D-0210	01 00 10.5	-33 50 42.0	1.03	1.30	3600	106	105	1.458
34	2018.09.09	SclC02	0101.D-0210	01 00 10.6	-33 36 41.5	1.14	1.00	4200	105	104	1.053
35	2018.09.17	SclC12a	0101.B-0189	01 00 00.0	-33 32 30.4	1.02	0.52	1700	85	52	1.272
-	2018.09.17	SclC12b	0101.B-0189	01 00 00.0	-33 32 30.4	1.01	0.66	3600	92	91	1.200
36	2018.09.17	SclC14	0101.B-0189	00 58 59.2	-33 49 20.0	1.05	0.72	4100	92	91	1.292
37	2018.09.17	SclC13	0101.B-0189	01 00 09.4	-33 50 19.6	1.20	0.64	4100	72	69	0.959
38	2018.09.17	SclC11	0101.B-0189	01 02 31.0	-33 38 49.4	1.16	0.52	3600	60	58	1.509
39	2018.09.18	SclC17	0101.B-0189	01 00 07.0	-33 44 11.4	1.06	1.26	4100	103	93	1.626
40	2018.09.19	SclC15	0101.B-0189	01 00 18.1	-33 45 59.1	1.06	0.63	4100	88	71	1.439
41	2018.09.19	SclC18	0101.B-0189	01 00 48.1	-34 10 58.9	1.22	0.78	3600	26	23	1.510
42	2018.09.19	SclC10	0101.B-0189	00 58 46.1	-33 05 29.4	1.04	0.56	3600	15	2	1.564
43	2018.09.19	SclC16	0101.B-0189	00 58 34.1	-33 36 00.0	1.01	0.43	3600	98	94	1.686
44	2018.12.15	Sclouter	0102.B-0786	00 57 34.9	-33 53 50.0	1.02	0.64	3600	39	37	0.821

Appendix B: Tests of the reliability of the measured v_{los} and EWs with VLT/FLAMES LR8

One observing programme in our collection (593.D-0309, PI: Battaglia) was a sequence of eight repeat observations of the same stars over 15 months, looking for velocity variability, and hence binary stars. Here to keep things simple only single pointings were compared to each other. These multiple VLT/FLAMES LR8 velocity and EW measurements of a sub-sample of 96 stars allow a test of the reliability (and repeatability) of velocity and EW measurements based on the CaT lines. We used these observations, typically with S/N> 20, to test our error analysis, and our measurement consistency between observations made at different epochs, being careful to ignore any obviously v_{los} variable stars (of which very few appear within our velocity sensitivity). A full analysis is in preparation by Arroyo Polonio et al. The fraction of binaries that they found is consistent with those expected from previous surveys.

Even though all the fields have the same setup, with the same guide and fiducial stars, and were mostly taken in good conditions, as is required for a monitoring programme, it is clear that some VLT/FLAMES observations are better behaved than others. Here we show an overview for a range of comparison plots. When the scatter in the S/N versus magnitude plot (Fig. B.1) is large, even at bright magnitudes, this is most likely due to variations in weather as well as a, perhaps related, poor astrometric alignment of the fibres compared to the guide stars. It is likely that there was a centring offset of the targets in the fibres, caused either by an imperfect astrometry of the guide stars – either intrinsically or relative to the targets – or an imperfect centring of the guide stars in their fibre bundles. This series of multiple measurements show how intrinsically hard it is to guarantee that guide and fiducial stars are centred correctly based on VLT/FLAMES pre-*Gaia* astrometry (Fig. B.1). The monitoring dataset does contain a range of atmospheric conditions, but there is no obvious correlation with seeing, although high air mass tended to produce poorer results, but S/N> 20 means all results were reliable most of the time, so the problems were only seen in low S/N measurements, which strongly suggests that misalignment is the problem, as it affects fainter stars more. The size and variation of the velocity shifts between fields were clearly much smaller and more stable once *Gaia* DR2 astrometry became available for both the targets and the guide stars and the fiducial stars for each observation. It is also worth noting that target acquisition at the telescope went much more smoothly with *Gaia* positions and proper motions. However, all the monitoring observations presented here were made pre-*Gaia*, so only later observations have benefited from *Gaia* astrometry.

The velocity errors were found to match the scatter in the velocities in repeat measurements of the same stars (Fig. B.2). The velocity scatter did not appear to change with S/N, and it should vary with 1/(S/N). This is consistent with the velocity scatter being limited by the accuracy of the wavelength solution and not the S/N for this relatively high S/N sample. Any stars that are beyond the 3σ scatter are potentially stars with intrinsically varying velocities, and thus likely binary systems (see Arroyo Polonio et al. in prep). The scatter was higher for the longer time baselines, but if this was due to slow variations intrinsic to a significant sub-sample of stars or a problem with the velocity stability over time it was not possible to say here. The intrinsic error on the velocity shifts applied to individual fields (as given in Table A.1) was given by the accuracy of the sky lines as velocity zero points, and this was ±1km/s for VLT/FLAMES LR8, and the observations tended to remain within this uncertainty. This correction likely dominated the offset velocity between fields, but the intrinsic measurement accuracy determines the scatter.

Likewise the EW scatter, and so the scatter in [Fe/H] determinations (Fig. B.3) were also stable, and did not change significantly with S/N. Thus, the measurements of [Fe/H] appeared to be limited by the errors in the continuum estimation, probably coming from scattered light in the images, and not the S/N. Both the offset and the scatter give a picture of the intrinsic measurement errors.

There was also no evidence of any strong effect from variations in airmass or seeing on velocity or EW measurements. In Fig. B.1 the top right hand panel, as can be seen from Table A.1, was observed at an airmass of 1.4, but there was no noticeable effect on the S/N, or the reliability of the repeated velocity and EW measurements. In Fig. B.1, the last panel (B8) looks particularly bad for no

obvious reason. In general the monitoring sample showed the consistency of the measurements, and thus provided an independent estimate of the measurement errors, which are found to be similar to previous investigations (e.g. Battaglia et al. 2008b), and were most reliable for S/N> 20. These plots highlight the intrinsic accuracy that can be achieved in the VLT/FLAMES LR8 spectroscopic measurements of velocity and [Fe/H] from night to night, both the zero point and the scatter.
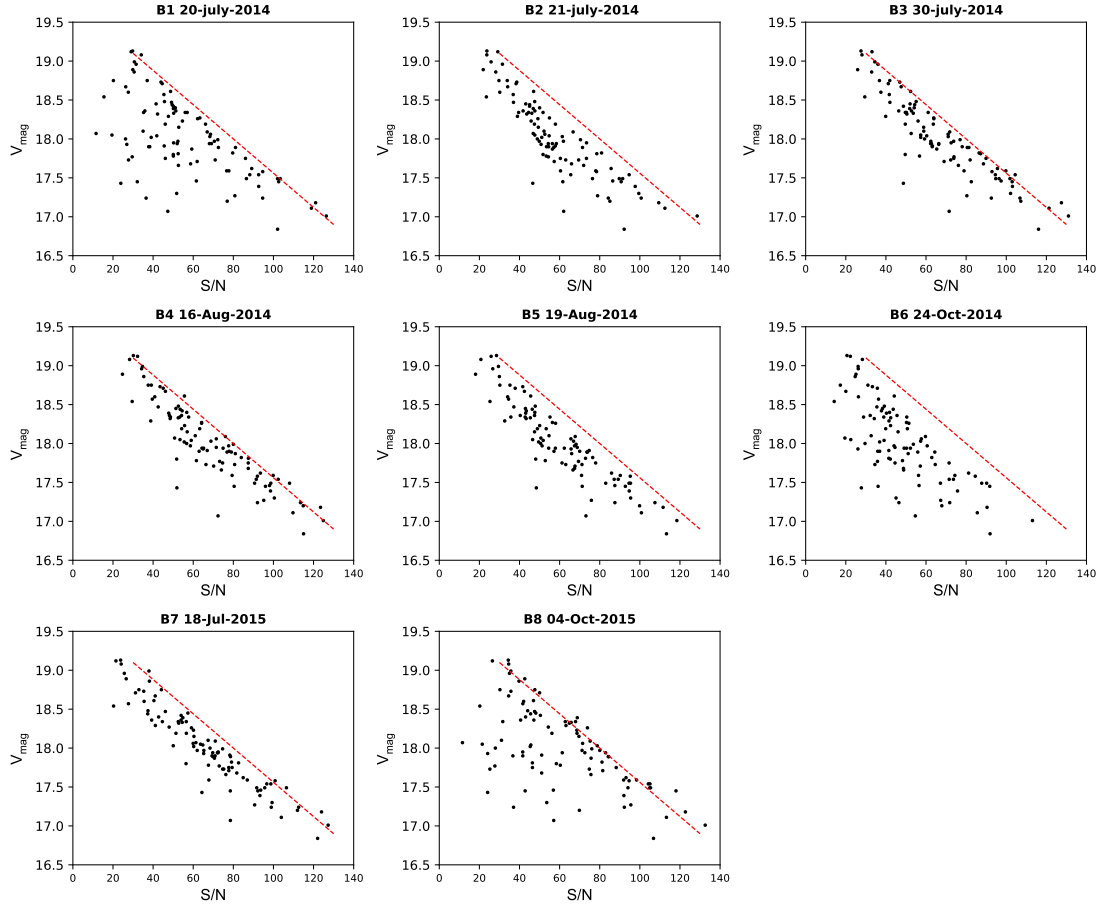

Fig. B.1. Variation in S/N for eight observations of the same field and the same targets with VLT/FLAMES LR8 grating. The dashed red line is always in the same position in each plot to guide the eye. The observations were made between July 2014 and October 2015 (from programme ID 593.D-0309)
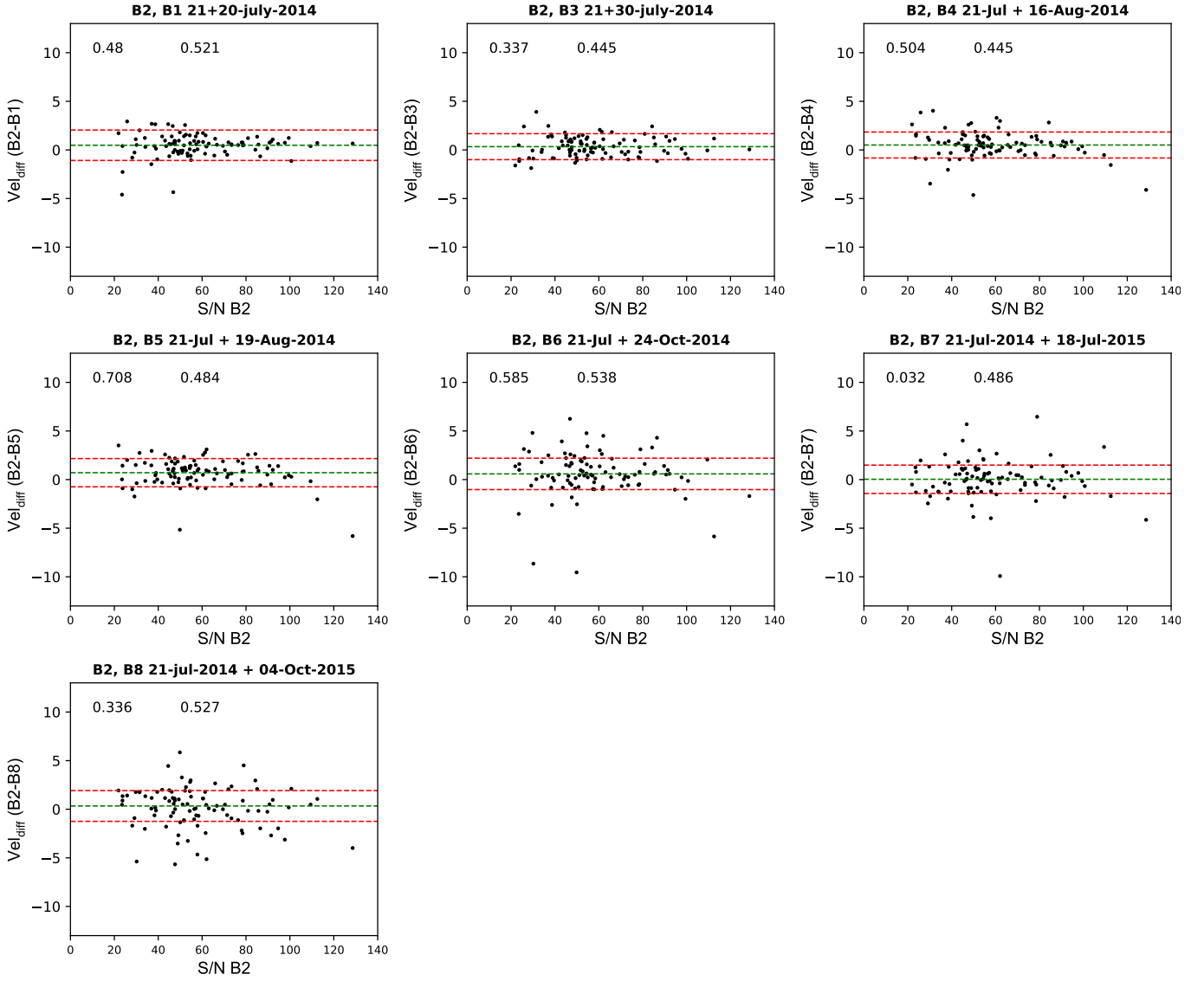
Fig. B.2. Comparison between the velocities measured for eight VLT/FLAMES LR8 observations of the same field and the same targets as a function of the S/N of the measurement. The observations were made between July 2014 and October 2015. All velocity measurements were compared with those from observation B2, which occurred on 21 July 2014. In the top of each plot the mean velocity offset and the variance for each comparison is given; the dashed green line is the mean, and the two dashed red lines on either side show 3σ about this mean.
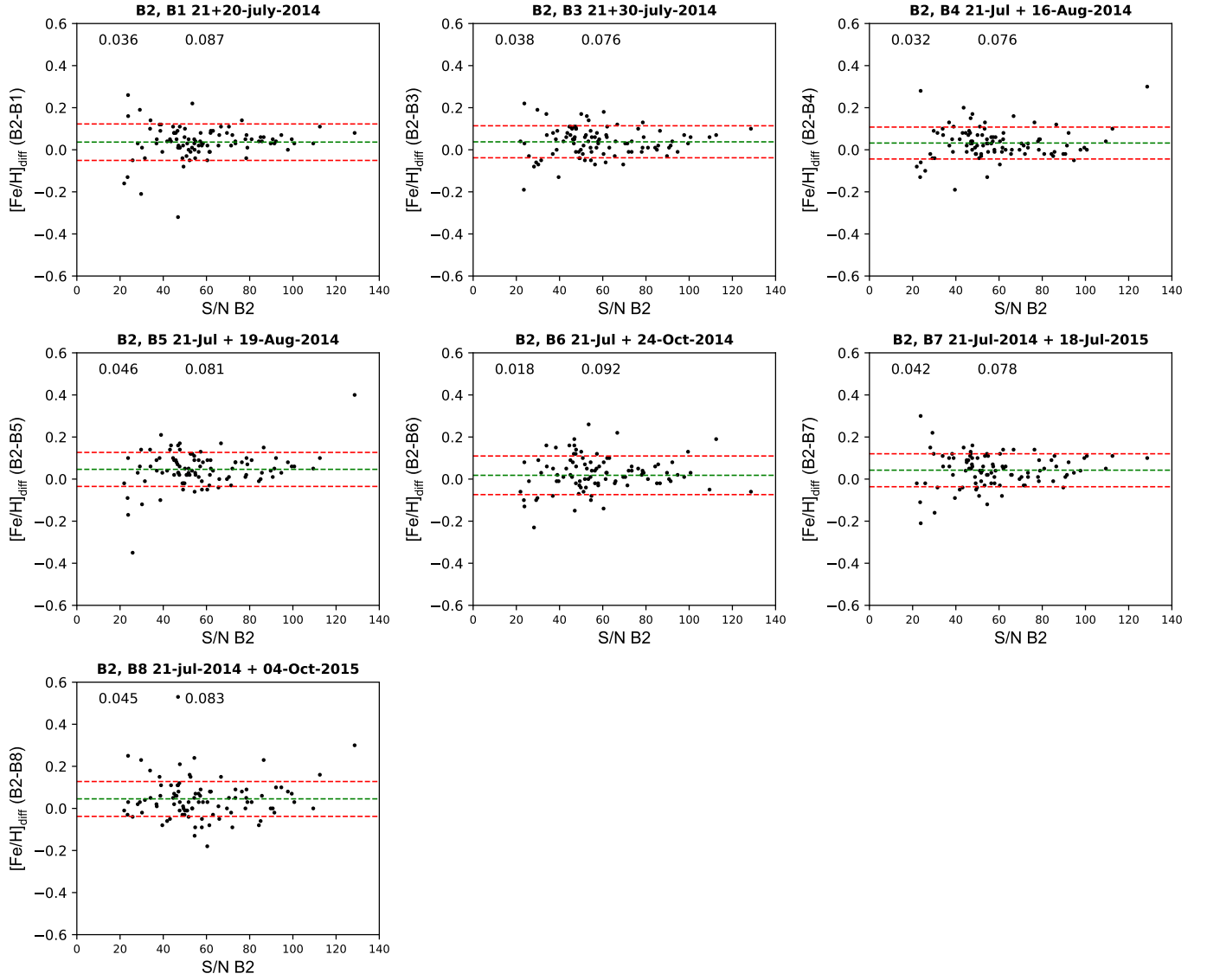
Fig. B.3. Comparison between [Fe/H] determined from EW measurements of the two strongest CaT absorption lines for eight VLT/FLAMES LR8 observations of the same field and the same targets as a function of the S/N of the measurement. The observations were made between July 2014 and October 2015. All [Fe/H] measurements were compared with those from observation B2, which took place on 21 July 2014. In the top of each plot the mean [Fe/H] offset and the variance is given for each comparison; the dashed green line is the mean, and the two dashed red lines on either side show 1σ about this mean.

Appendix C: A comparison between CaT [Fe/H] and direct high resolution [FeI/H] measurements

A subsample of the metallicities ([Fe/H]) determined using the CaT triplet lines in this paper, were compared with the VLT/FLAMES HR measurements, which were based on numerous individual Fe I and Fe II lines (Hill et al. 2019, see our Fig. C.1). We used *Gaia* photometry converted to the V magnitude (Riello et al. 2021) applied to the metallicity conversion from EWs into [Fe/H] coming from (Starkenburg et al. 2010). This is not the photometry that was originally assumed, so this may be the origin of a small offset of 0.1 dex between [Fe/H] measured from HR10 and that from LR8, such that LR8 metallicities were 0.1 dex more metal rich than the HR measurements. There was no trend in the scatter with the magnitude of the star, nor with the changing [Ca/H], so the scatter may simply be that which could be expected due to the calibration and inherent uncertainties in the different methods.

In Fig. C.1b we show the radial velocities measured with VLT/FLAMES HR10 compared to those measured with VLT/FLAMES LR8. The comparison looks very good, without any need for offset. There are a few outlying points, which might suggest velocity variability with time.

In Fig. C.2 we show how the comparison between the different methods of measuring [Fe/H] depend on the luminosity of the star (G mag) and also the [Ca/H] measured by Hill et al. (2019). There does not seem to be a strong trend with either magnitude or [Ca/H]. However, there are patterns, with scatter, that may suggest the known effect that the CaT determination of [Fe/H] also depends weakly on [Ca/H] (Starkenburg et al. (2010)).
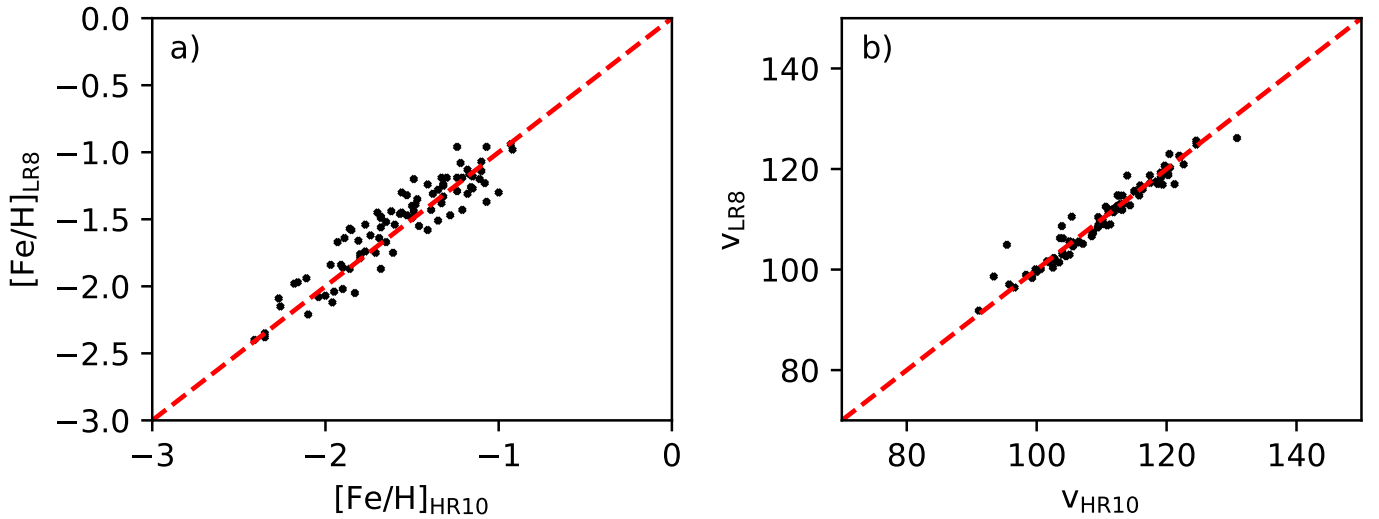

Fig. C.1. Comparison between VLT/FLAMES HR10 measurements and VLT/FLAMES LR8 measurements of (a) [Fe/H] and (b) the los radial velocities.

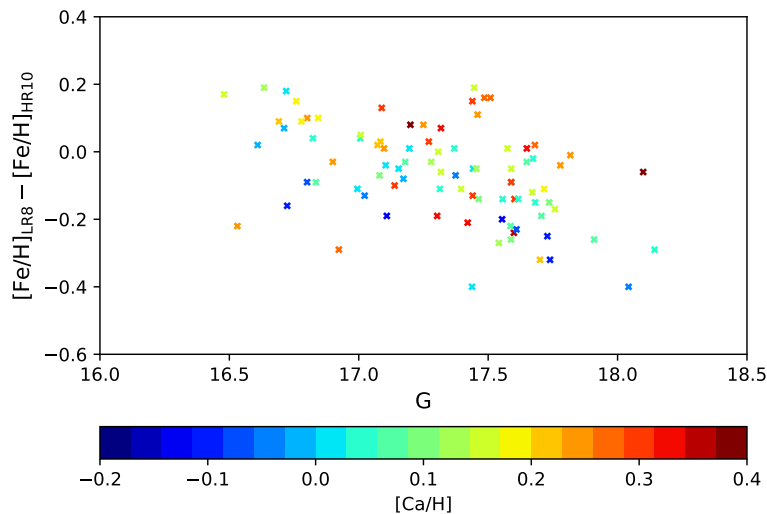**Fig. C.2.** Comparison between VLT/FLAMES HR10 measurements and VLT/FLAMES LR8 measurements of [Fe/H], colour coded by [Ca/H] from VLT/FLAMES HR abundance determinations.

Appendix D: *Gaia* archive query for the Sculptor field

Here we give, in Astronomical Data Query Language. the query to be executed in the *Gaia* archive, that extracts all sources in the Sculptor field with parallaxes, proper motions, and a $(G_{BP} - G_{RP})$ colour. The query also retrieves the distance estimates from Bailer-Jones et al. (2021) and contains an on-the-fly calculation of the corrected flux excess factor C^* (Riello et al. 2021). The J2000.0 ICRS position and proper motion of Sculptor are as listed in the Set of Identifications, Measurements, and Bibliography for Astronomical Data (SIMBAD; Wenger et al. 2000) and are propagated in the query to J2016.0, the reference epoch for *Gaia* DR3. The selected field is two degrees in radius around the Sculptor centre.

```
select gaia.*,
if_then_else(
    gaia.bp_rp > -20,
    to_real(case_condition(
        gaia.phot_bp_rp_excess_factor - (1.162004 + 0.011464*gaia.bp_rp
                                + 0.049255*power(gaia.bp_rp,2)
                                - 0.005879*power(gaia.bp_rp,3)),
        gaia.bp_rp < 0.5,
        gaia.phot_bp_rp_excess_factor - (1.154360 + 0.033772*gaia.bp_rp
                                    + 0.032277*power(gaia.bp_rp,2)),
        gaia.bp_rp >= 4.0,
        gaia.phot_bp_rp_excess_factor - (1.057572 + 0.140537*gaia.bp_rp)
    )),
    gaia.phot_bp_rp_excess_factor
) as phot_bp_rp_excess_factor_corr,
cbj.r_med_geo, cbj.r_lo_geo, cbj.r_hi_geo, cbj.r_med_photogeo,
cbj.r_lo_photogeo, cbj.r_hi_photogeo
from gaiadr3.gaia_source as gaia
join external.gaiaedr3_distance as cbj
using(source_id)
where
contains(
    point('ICRS',gaia.ra,gaia.dec),
    circle(
        'ICRS',
        COORD1(EPOCH_PROP_POS(15.039169999999999,-33.70889,0,
                        .0900,.0200,111.4000,2000,2016.0)),
        COORD2(EPOCH_PROP_POS(15.039169999999999,-33.70889,0,
                        .0900,.0200,111.4000,2000,2016.0)),
        2)
)=1 and
gaia.astrometric_params_solved >3 and gaia.bp_rp is not null
```

Appendix E: The Results

Here we show an example of what is available as an online table at CDS for the combined *Gaia* DR3 photometry and astrometry and VLT/FLAMES LR8 spectroscopy for stars in and around the Sculptor dSph. In Table E.1 we show the full VLT/FLAMES LR8 sample, and the combination with *Gaia* DR3 astrometry, including those likely velocity members that are in fact non-members. In Table E.2 we also include the VLT/FLAMES LR8 velocity non-members as a matter of interest, including only the measured velocities and their *Gaia* DR3 IDs.

The stars in Table E.2 were immediately identified as v_{los} non-members by the VLT/FLAMES spectroscopy and removed from any further analysis.

Table E.1. *Gaia* DR3 and VLT/FLAMES results for stars in and around the Sculptor dSph.

| GaiaDR3Id | Gaia-RA | Gaia-DEC | Gaia-G | Gaia-BP | Gaia-RP | plx | plx-err | pmra | pmra-err | pmdec | pmdec-err | ellr |
Flamesfield	SpecName	N-Spec	SN	Vel	vel-err	vel-var	FeH	feh-err	feh-var	z	mem	feh-rel
5003449261308998016	13.6648395642	-33.5229968216	18.122	18.6056	17.478	0.0258	0.1224	0.094	0.12	-0.224	0.167	1.1596
2007.gb202a	scl011_09_	2	52.97	119.59	0.418	0.455	-2.46	0.065	0.074	0.162	m	0
5003436483781148928	13.7546852173	-33.5733720453	19.875	20.3454	19.2269	-0.0662	0.3705	0.728	0.459	-0.795	0.597	1.0788
2007.gb202a	scl034_11_	2	17.02	105.59	1.49	3.209	-2.15	0.235	0.288	5.459	m	0
5003383977805922560	13.8745180848	-33.7683070902	18.2596	18.7467	17.5758	0.153	0.147	0.008	0.126	-0.279	0.186	0.9977
2003.Scl11a	scl_11_040	3	25.33	119.23	0.964	3.043	-2.74	0.172	0.169	1.389	m	0

Notes. The columns are: GaiaDR3Id, *Gaia* DR3 Id number; Gaia-RA, RA (deg); Gaia-DEC, Dec. (deg); Gaia-G, *Gaia* DR3 G magnitude; Gaia-BP, *Gaia* DR3 G_{BP} magnitude; Gaia-RP, *Gaia* DR3 G_{RP} magnitude; plx, *Gaia* DR3 parallax; plx-err, *Gaia* DR3 error on the parallax; pmra, *Gaia* DR3 proper motion in RA direction; pmra-err, *Gaia* DR3 error on RA proper motion; pmdec, *Gaia* DR3 proper motion in Dec. direction; pmdec-err, *Gaia* DR3 error on Dec. proper motion; ellr, elliptical radius at which the star lies; Flamesfield, name of the VLT/FLAMES pointing; SpecName, name of object in VLT/FLAMES pointing; N-Spec, number of individual VLT/FLAMES spectra combined; SN, the signal-to-noise of the single (for N-Spec=1) or combined VLT/FLAMES spectra; Vel, the v_{los} for this star measured from VLT/FLAMES spectra, averaged if N-spec> 1; vel-err, error on the v_{los} VLT/FLAMES measurement; vel-var, the variance of the VLT/FLAMES v_{los} if N-spec> 1; FeH, the [Fe/H] for the star determined from the CaT measurement from VLT/FLAMES spectra, averaged if N-spec> 1 ; feh-err, the error on the VLT/FLAMES [Fe/H] determination; feh-var, the variance of the VLT/FLAMES [Fe/H] if N-spec> 1; z, the *Gaia* DR3 membership score, as defined in Sect. 3.1; mem, the likely membership of the star in the Sculptor dSph where m is for member stars, b is for borderline members and n is for non-members; feh-rel gives the reliability of the [Fe/H] determination, where 0 is for reliable [Fe/H] and 1 is for an unreliable [Fe/H], which should be used only with great caution, for non-member stars a CaT [Fe/H] has no meaning, and so these are given as – in this column and there are also no values given in the table. The non-members in Table E.1 are stars with VLT/FLAMES spectroscopic v_{los} compatible with membership in Sculptor but the *Gaia* proper motions and/or parallaxes ruled this out.

Table E.2. VLT/FLAMES spectroscopic non-members of the Sculptor dSph.

GaiaDR3Id	RA	Dec	Flamesfield	SpecName	vmag	sn	vel
5026428298415447808	15.91929167	-33.79244444	2004.Scl14a	scl_14_050	18.31	25.686	25.26
5027198781189387520	15.80508333	-33.51108333	2004.Scl14b	scl_14_064	19.23	19.638	63.48